

Active Cavity Optomechanics Based on Phonon-Induced Light-Matter Interactions

Chenjiang Qian,^{1,*} Viviana Villafaña,¹ Martin Schalk,¹ Georgy V. Astakhov,² Ulrich Kentsch,² Manfred Helm,² Pedro Soubelet,¹ Andreas V. Stier,¹ and Jonathan J. Finley^{1,†}

¹Walter Schottky Institut and Physik Department,

Technische Universität München, Am Coulombwall 4, 85748 Garching, Germany

²Helmholtz-Zentrum Dresden-Rossendorf, Institute of Ion Beam Physics and Materials Research, 01328 Dresden, Germany

We investigate the interaction between optically excited charged boron vacancies V_B^- , localized photonic modes of ultra-high-Q ($\sim 10^5$) nanocavities and local vibronic modes. V_B^- is a color center for which phonon-induced processes generally dominate the emission. A pronounced asymmetry is observed in the emission spectrum for cavities in which V_B^- centers have been generated by N^+ irradiation. Similar asymmetries are not observed for systems that do not contain V_B^- centers. To explain our findings, we model the system as phonon-induced light-matter coupling with multi-partite interplay between the electronic transition, cavity photons and local vibronic modes. Good agreement is obtained between experiment and theory. Our results indicate that the multi-partite interplay arises during the V_B^- emission process, illustrating that it is phonon-induced, rather than being caused by thermal population of vibronic modes. The multi-modal couplings between various photonic (V_B^- emission, cavity nanophotonic) and vibronic (V_B^- phonons, cavity nanomechanical) modes provide novel method to interface spin, photons and phonons in condensed matter systems.

I. INTRODUCTION

Hexagonal boron nitride (hBN) is a wide bandgap 2D semiconductor that has recently been found to host a variety of optically active point defects of interest for single photon generation, spin-photon interfaces and quantum sensing [1–6]. The negatively charged boron vacancy V_B^- attracts particular interest, due to its paramagnetic nature and spin-dependent optical properties at room temperature [4–8]. The emission from V_B^- is dominated by phonon-induced processes, indicative of strong electron-phonon coupling involved in the radiative decay [9–12]. In addition, hBN has good thermal and chemical stability and can be readily integrated into high-Q nanophotonic cavities [12–15]. The electronic and optical properties of hBN are highly sensitive to local deformations caused e.g., by excitation of nanomechanical vibrations [16–21]. Therefore, by creating V_B^- centers in an hBN nanocavity that simultaneously supports localized photonic and vibronic modes [22–24], we realize an emitter-optomechanical system in which V_B^- related phonons bridge the coupling between V_B^- emission, cavity photons and cavity vibrations.

Here, we investigate the emitter-optomechanical interaction in the cavity- V_B^- system using spatially resolved photoluminescence (PL) and Raman spectroscopy. We observe a pronounced spectral asymmetry of the ultra-high-Q ($\sim 10^5$) cavity photonic mode that only presents for nanobeam cavities in which V_B^- centers have been created via ion beam irradiation [12, 25, 26]. We construct a numerical model in which coupling is induced between emitter, cavity photon and local vibronic modes during the decay process of V_B^- . Our model accounts

well for the asymmetry arising from V_B^- -induced photon-phonon coupling. Similar asymmetries are not observed for non-irradiated cavities supporting our interpretation that the coupling is not mediated by thermally excited phonons, but rather induced by phonons generated during the V_B^- emission process itself [9–12]. Furthermore, we demonstrate the strong interaction between optomechanical cavity modes and phonon-induced V_B^- emission by spatially correlating luminescence in freely suspended structures [21] and the resonant excitation of cavity photons [27]. In position-dependent measurements, we observe anticrossings between the V_B^- emission peaks induced by the nanomechanical vibrations. When subject to resonant excitation, the Raman signal of V_B^- phonons exhibits an asymmetric enhancement at the cooling and heating detunings [27], demonstrating the cavity vibrations induce the coupling between V_B^- phonons and cavity photons. Such multi-modal couplings in the emitter-optomechanical system provide new paradigm for tailoring the interface [28] between spin defects, photons and phonons in condensed matter systems.

II. RESULTS AND DISCUSSIONS

The structure of our hybrid hBN/Si₃N₄ nanobeam cavity is schematically depicted in Fig. 1(a). Detailed fabrication procedures have been reported previously [12, 15] and are also presented in supplement. The confinement of photons in quasi 0D photonic modes is achieved by locally chirping the photonic crystal periodicity at cavity center. Besides discrete photonic modes, the cavity also supports vibronic modes since the hBN/Si₃N₄ nanobeam is freely suspended but clamped at both ends [22–24]. Representative localized photonic and vibronic modes are depicted in Fig. 1(b) in blue and orange, respectively. In Sample-A, selected nanobeam cavities are irradiated by 30 keV N^+ ions with a fluence (dose) of

* chenjiang.qian@wsi.tum.de

† finley@wsi.tum.de

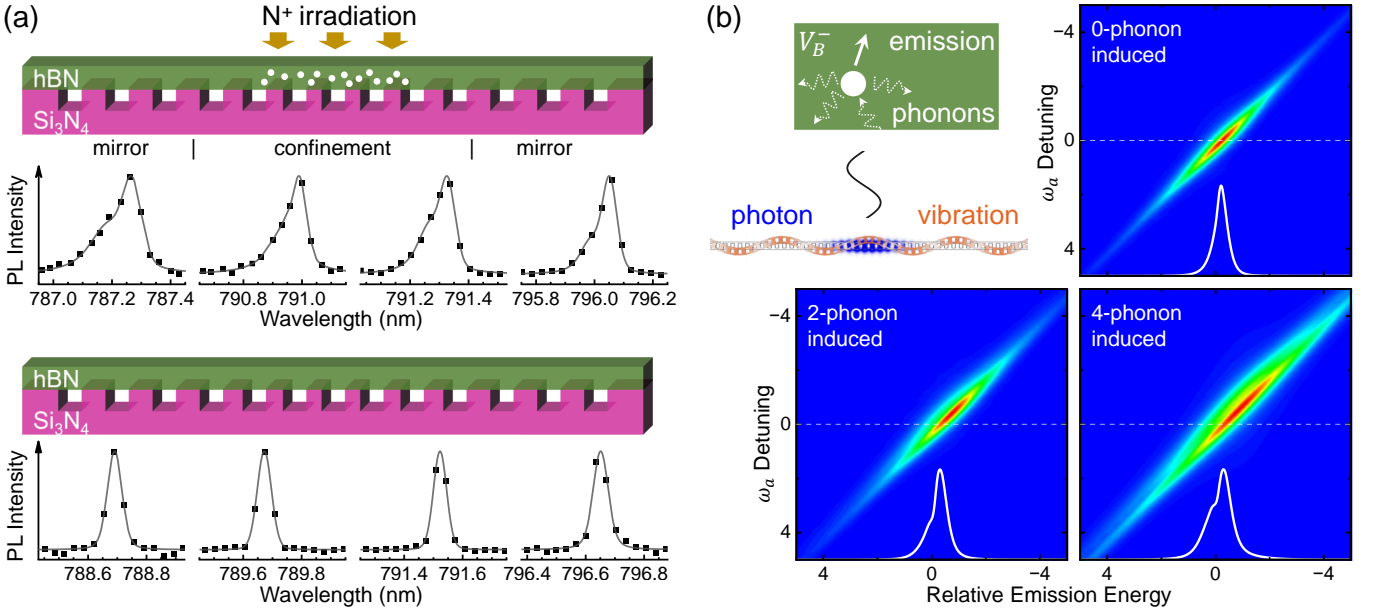


FIG. 1. (a) Schematic of cavity structure and irradiated region for Sample-A. The irradiated cavities exhibit a pronounced asymmetric lineshape arising from the photon-phonon coupling. In contrast, no asymmetry is observed when the hBN is not irradiated. (b) The V_B^- is dominated by phonon-induced emission. The cavity supports photonic and vibronic modes. Thereby, the system involves multi-partite interplay between V_B^- emission, phonons associated with V_B^- , cavity photons and cavity vibrations. We calculate spectra in the cases of emitter-photon coupling induced by zero, two and four phonons. White lines are the spectra at resonant $\omega_a = \omega_X$ for examples. The phonon-induced processes clearly enhance the asymmetric of cavity emission lineshape.

10^{13} ions/cm² to create boron vacancies within the volume of photonic mode (Fig. 1(a) upper). V_B^- exhibits bright emission dominated by phonon-induced processes, whilst the zero-phonon emission at ~ 773 nm is weak [9–12]. In contrast to emitters dominated by zero-phonon emission, the role of electron-phonon interactions in V_B^- emission is intrinsically strong. This gives rise to a spectrally broad emission, even at low temperature [5], and coupling of vibronic modes to the dipole allowed optical transitions associated with the V_B^- center. Thus, local vibronic modes of the nanobeam cavity may be expected to impact on the phonon-induced V_B^- emission, and the cavity- V_B^- system involves couplings between dipole allowed electronic transitions, defect phonons, cavity photons and cavity nanomechanical vibrations, as a multi-modal emitter-optomechanical system depicted schematically in Fig. 1(b).

We begin by comparing the spectral form of the emission observed from the cavities with and without irradiation. All cavities were excited using a 532nm cw-laser having a spot size $\sim 1 \mu\text{m}$ and a power $\sim 120 \mu\text{W}$. The cavity photonic mode is hence excited by emission from the V_B^- centers in hBN (irradiated) and/or filtered light arising from other native luminescent defects in the hBN and underlying Si_3N_4 (non-irradiated). The cavity mode exhibits high Q value $\sim 10^5$ limited only by the spectral resolution of our detection system [15]. Remarkably, for the N^+ irradiated cavities we observe a strongly asymmetric lineshape of cavity emission that is broadened on

the short wavelength (high energy) side. Typical spectra recorded from four representative cavities with or without irradiation are presented in the upper and lower panels of Fig. 1(a). These data are representative of all irradiated (non-irradiated) high-Q ($\geq 10^4$) cavities investigated. The lineshape asymmetry is, however, masked in lower-Q ($< 10^4$) irradiated cavities (see supplement). We identify the asymmetric peaks as arising from strong photon-phonon coupling [27, 30, 31]. To quantitatively account for the spectral asymmetry, we develop a model in which a 2-level emitter simultaneously couples to cavity photons and local phonons. The Hamiltonian of the multi-modal cavity QED system can then be written as

$$\begin{aligned}
 H = & \hbar\omega_X\sigma_{X,X} + \hbar\omega_a a^\dagger a + \hbar\omega_q q^\dagger q \\
 & + \hbar\lambda_{e-q}\sigma_{X,X}(q + q^\dagger) + \hbar\lambda_{p-q}a^\dagger a(q + q^\dagger) \\
 & + H_{e-p}
 \end{aligned}$$

including the 6 terms corresponding to the emitter, photon, phonon, emitter-phonon coupling with a strength λ_{e-q} , photon-phonon coupling with a strength λ_{p-q} , and emitter-photon coupling, respectively [32]. $\sigma_{A,B}$ ($A, B \in \{X, G\}$) is the Dirac operator for the emitter with the ground (G) and excited (X) state, a^\dagger/a are the ladder operators for cavity photons, and q^\dagger/q are the ladder operators for phonons. Since the V_B^- emission is dominated by phonon-induced processes [9–12], we introduce an effective *phonon-induced* emitter-photon coupling

$$H_{e-p} = \hbar g \left(\sigma_{G,X} (q^\dagger)^k a^\dagger + \sigma_{X,G} q^k a \right)$$

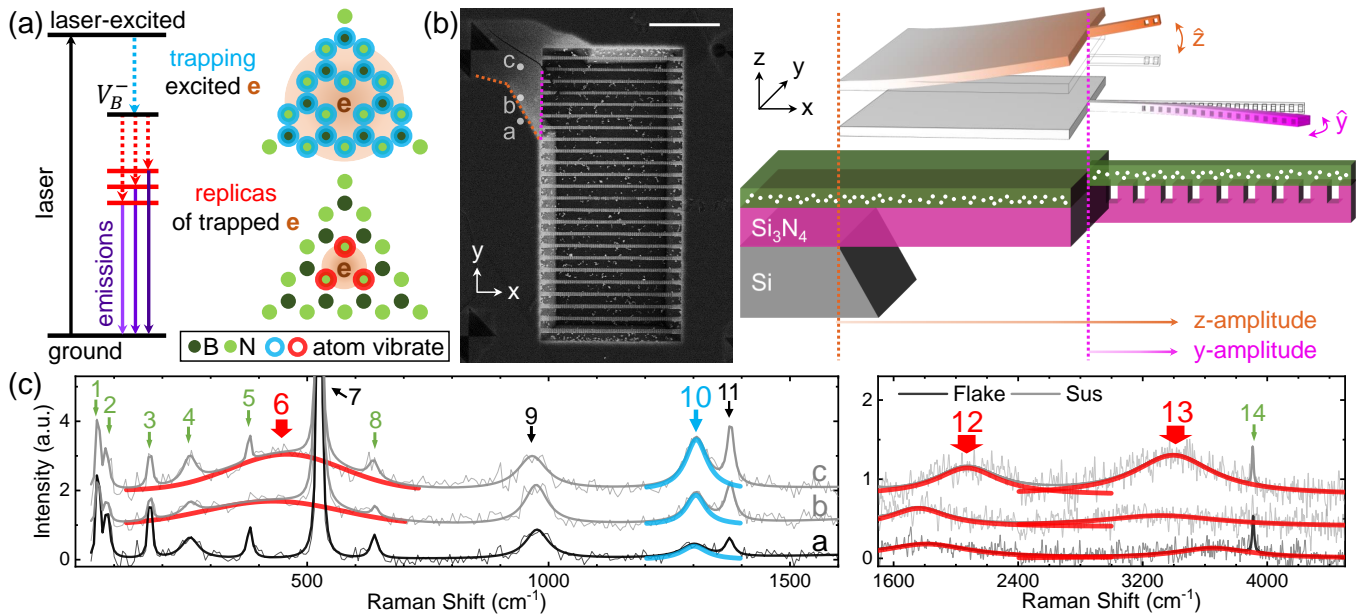


FIG. 2. (a) Schematic representation of the V_B^- excitation, thermalisation and emission processes: due to the spatial overlap between the electron wavefunction (brown shade) and the atoms involved in the local phonon modes (blue or red rings), the extended phonons from the defect complex (blue rings) are expected to dominate the trapping process (blue dashed arrow), and the highly localized phonons (red rings) dominate the replica processes (red dashed arrows). (b) SEM image of Sample-B, including the large suspended membrane (upper left) and an array of nanobeam cavities (middle). The white scale bar is 10 μm . The sample structure and corresponding nanomechanical modes are schematically depicted in the upper right. (c) Typical Raman spectra recorded from positions a - c shown on (b). Phonon modes 1-14 are observed in the three positions. Peak 10 (blue) is the extended phonon [29]. Broad peaks 6, 12 and 13 (red) are highly localized phonons [29] and are the only ones exhibiting distinguishable position-dependent energy shift in this work.

where g is the coupling strength and k is the number of phonons involved the coupling. $k = 0$ corresponds to the conventional Jaynes-Cummings model applied for usual emitters dominated by zero-phonon line emission, where the phonons only introduce vibronic sublevels to mediate the emitter-photon coupling, but do not directly participate. In contrast, H_{e-p} with $k \geq 1$ represents an entirely different but coherent interface of emitter, photon and phonon, in which the phonon is necessary to induce the emitter-photon coupling.

We calculated the spectral form of the emission from the cavity photonic mode by solving the master equation (for details see supplement). Typical spectra in the case of $k = 0, 2$ and $k = 4$ are presented in Fig. 1(b), respectively, as the detuning between the energy of the 2-level emitter and the cavity mode is varied. The white curves show the spectral form at resonance $\omega_a = \omega_X$, illustrating the evolution from a symmetric lineshape ($k = 0$) to a clearly asymmetric lineshape induced by H_{e-p} with $k > 0$. The asymmetry in the emission lineshape is suppressed for $k = 0$ but becomes more pronounced as k increases from 2 to 4. Despite the model being rather simple, it provides a very good qualitative description of our experimental observation. As presented in Fig. 1(a), we do not observe any asymmetry in any of our control experiments for which the hBN was not irradiated with N^+ . This is the central result of this work, showing that

the phonons involved in the photon-phonon coupling are not thermally excited, but rather arise *during* the emission from V_B^- centers. As such, they give rise to a novel emitter-induced opto-mechanical coupling.

Generally, as schematically depicted in Fig. 2(a), two different phonon processes are involved in the V_B^- emission when non-resonantly excited. The blue dashed arrow involves creating the negatively charged electronic state of V_B^- by trapping an excited electron that relaxes via phonon assist [33, 34], before recombining again with the participation of localized phonons as denoted by the red dashed arrows. The recombination processes give rise to the phonon replica sidebands in the PL spectrum, denoted by the purple arrows. Since V_B^- emission is dominated by the phonon sidebands [9–12], the wavelengths of emission peaks are determined by the energy and mean number of phonons in the replica process. The electron-phonon spatial overlap [35, 36] depicted schematically in Fig. 2(a) indicates that, extended phonons involving the vibration of multiple atoms around the defect (blue rings on Fig. 2(a)) govern the trapping process, whilst more highly localized phonons involving only the vibrations of neighboring atoms (red rings) dominate the replica process. J. Li et al. [29] recently reported Raman spectroscopy of V_B^- centers and unveiled this picture for extended phonons and highly localized phonons via boron isotope characterization.

To confirm this picture for V_B^- emission in Fig. 2(a) and the interaction with vibronic modes in nanocavities, we recorded spatially resolved PL and Raman spectroscopy from another sample (Sample-B) that is homogeneously irradiated by 30 keV N^+ ions with a fluence (dose) of 10^{14} ions/cm² [12, 25, 26] as shown in Fig. 2(b). Sample-B contains three different regions of interest: (i) the non-underetched region with hBN on a planar Si_3N_4/Si substrate corresponding to the dark surrounding region in the SEM image, (ii) the large suspended membrane with hBN/ Si_3N_4 layers suspended on underetched Si corresponding to the large bright regions at left top, and (iii) suspended cavities with a varying nanobeam width d_y . No cavity photonic mode exists in the large suspended membrane or the nanobeam edges. Instead, as depicted schematically in Fig. 2(b), the two regions have vibronic modes with amplitudes determined by the position relative to the clamping points. These vibronic modes have frequencies in the range 10 to 200 MHz [24]. As shown in Fig. 2(b), the large suspended membrane primarily supports out-of-plane (z-) vibronic modes, and the nanobeam supports both out-of-plane and in-plane (y-) modes. Therefore, optomechanical effects on V_B^- emission through in- and out-of-plane modes can be identified by comparing the spatially resolved PL and Raman spectra recorded from these three regions.

Representative Raman spectra recorded from one position (labelled *a*) in the non-underetched region and two positions (labelled *b* and *c*) in the large suspended membrane are presented in Fig. 2(c). The observed Raman features are labelled 1-14 as denoted on the figure. Peaks 7 at 524 cm⁻¹ and peak 9 at 975 cm⁻¹ are the bulk Si_3N_4 phonons [37]. Peak 11 at 1377 cm⁻¹ is the bulk hBN phonon E_{2g} [29]. The other peaks are not observed in Si_3N_4 nor non-irradiated hBN (see supplement). Hence, we identify them as from V_B^- centers. Peak 6 around 450 cm⁻¹ (red curve) is the highly localized phonon, and peak 10 at 1306 cm⁻¹ (blue) the extended phonon discussed in the context of Fig. 2(a), which have been previously identified [29]. We observe two other broad Raman features with higher energies: peak 12 around 1800 cm⁻¹ (quadruple of peak 6) and peak 13 around 3600 cm⁻¹ (double of peak 12). The broader Raman linewidth typically implies stronger spatial confinement of the phonon mode [38–40]. In addition, peaks 6, 12 and 13 are the only V_B^- phonons exhibiting distinguishable energy shifts, when moving the laser spot e.g., between the three positions in Fig. 2(c). These common features indicate that peaks 12 and 13 stem from multi-phonon states of peak 6 and are also highly localized at the V_B^- center. The other Raman peaks 1-5, 8 and 14 at 67, 86, 174, 256, 382, 638, 3909 cm⁻¹ exhibit little energy shift between different detection positions, and their intensity variation does not follow the PL intensity of any V_B^- emission peak. Thus, we suggest that they stem from the acoustic or out-of-plane optical phonons [41] and do not discuss them further here.

In Fig. 3(a)(b) we present the Raman and PL spec-

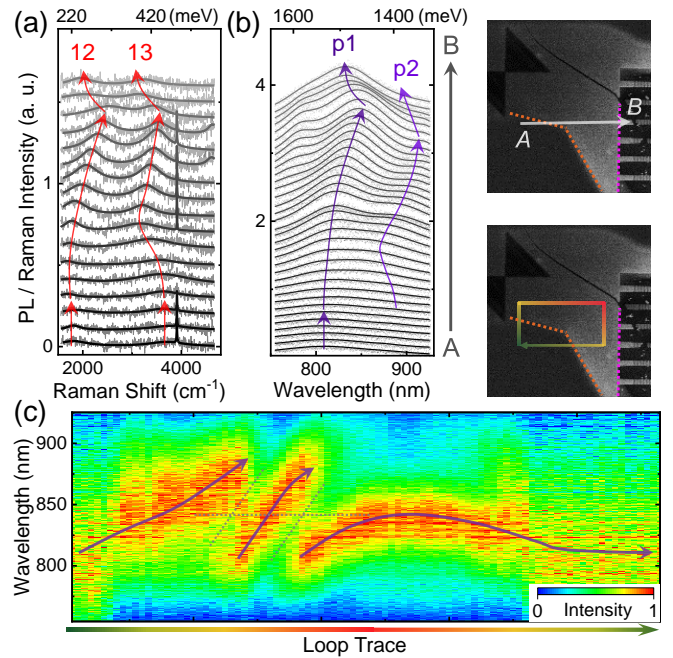


FIG. 3. Spatially resolved Raman (a) and PL (b) spectra recorded from positions along the line $A \rightarrow B$ in the inset. (c) Map of normalized PL spectra extracted from a loop trace shown in the inset. Anticrossing is clearly demonstrated, otherwise the PL peak cannot shift back after the loop.

tra of V_B^- centers recorded from positions along the line $A \rightarrow B$ denoted in the inset, respectively. The contour includes three regions that begins with hBN on a non-underetched region of the sample, before moving onto the large suspended membrane and nanobeam. Position-dependent energy shifts of the Raman and PL peaks in the three regions are denoted by the three-stage arrows and exhibit remarkable correlations, i.e. the shifts of Raman peaks 12 and 13 in Fig. 3(a) track the shifts of PL peaks p1 and p2 in Fig. 3(b). This observation strongly suggests that peaks p1 and p2 observed in PL are phonon sidebands arising from the highly localized phonon modes represented by Raman peaks 12 and 13 (red dashed arrows in Fig. 2(a)). Moreover, we find that the position-dependent shifts of V_B^- phonons and emission peaks do not arise from simple continuous shifting but rather exhibit pronounced anticrossings. Figure 3(c) shows a series of PL spectra recorded when traversing a closed clockwise loop on the sample as denoted in the inset. As depicted by the dashed lines on Fig. 3(c), two pronounced anticrossings are observed at which one spectral feature disappears and is replaced by another. The observation of such anticrossings combined with the fact that the spectra are identical at the beginning and end of the loop provide strong evidence for the anticrossings induced by couplings between different vibronic modes. Similar features and anticrossings between highly localized phonons are also observed from the Raman spectra (see supplement), further supporting this conclusion.

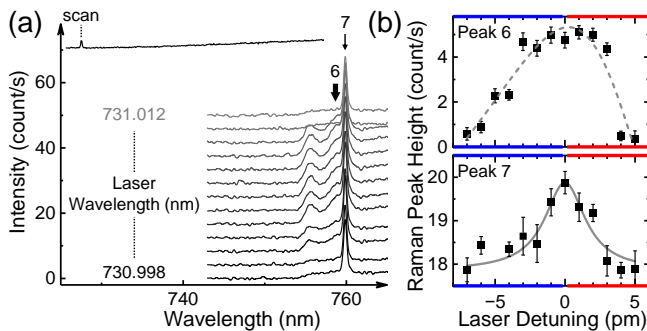


FIG. 4. (a) Resonant excitation of a cavity photonic mode. Top is the PL spectrum excited by 532nm laser with the scanned mode denoted. (b) The asymmetric enhancement of V_B^- phonons peak 6 is strong (weak) as the cavity vibrations heated (cooled) at blue (red) detunings. In contrast, the enhancement of Si_3N_4 phonon peak 7 is nearly symmetric.

The observed position dependencies of the Raman and PL spectra in Fig. 3(a)(b) reveal that the primary out-of-plane vibronic modes in the large suspended membrane (second-stage) enhance the total PL intensity and red shift the PL peak p1, whilst the in-plane vibronic modes in the nanobeam (third-stage) have the opposite effect. These characteristic impacts of in- and out-of-plane vibronic modes are further found to be consistent with the emission of V_B^- recorded on freely suspended nanobeam cavities that span between non-underetched regions. In those nanobeams, the local vibration involves a superposition of in- and out-of-plane modes, thus the V_B^- emission depends on the nanobeam width d_y since the bending rigidity varies with d_y [42]. These additional explorations are discussed in detail in supplement.

Finally, we explore the emitter-optomechanical interaction by controlling the optomechanical cavity modes via resonant excitation of the cavity itself. Hereby, the spectrum is detected as a narrowband ($\leq 1\text{MHz}$) cw-laser is tuned between 730.998 and 731.012 nm over an ultra-high-Q cavity photonic mode centered at 731 nm. Typical results obtained from such resonant excitation spectroscopy are presented in Fig. 4(b) that shows the Raman peaks 6 and 7 as the function of laser-cavity detuning. The population of photons in the cavity is enhanced at both red and blue detunings. The enhanced cavity photons couple to the phonons of Si_3N_4 and V_B^- thus enhance the corresponding Raman signals [43]. In contrast, the population of cavity vibronic modes is reduced at red detunings (cooling) while enhanced at blue detunings (heating) [27]. As presented in Fig. 4(b), the enhancement of peak 6 arising from V_B^- phonon is pronounced, varying by $> 10\times$ as the laser is tuned over the

cavity mode. Moreover, this enhancement is asymmetric with respect to detuning, being weaker with the cooling of cavity vibrations (red detuning) whilst being stronger with the heating (blue detuning). This observation reveals that the cavity vibrations induce the coupling between cavity photons and V_B^- phonons [24]. In contrast, the enhancement of peak 7 arising from Si_3N_4 phonon is much weaker (10%) and nearly symmetric, indicating that the cavity photons directly couple to Si_3N_4 phonon without the participation of cavity vibronic modes.

III. CONCLUSIONS

In summary, we report the multi-modal couplings between different photonic (V_B^- emission, cavity nanophotonic) and vibronic (V_B^- phonon, cavity nanomechanical) modes in the cavity- V_B^- system. The PL and Raman spectroscopy demonstrate the emitter-induced cavity optomechanics and the optomechanical-induced control of V_B^- emission and phonons. For usual emitters dominated by zero-phonon emission, their mechanical coupling effects are relatively weak and thereby, usually studied in an acoustic cavity (only supports vibronic modes) subjected to strong external drive [44, 45]. In such system the coupling to cavity photonic modes or other degrees of freedom is limited. In contrast, V_B^- is dominated by phonon-induced emission [9–12]. Our theoretical model and experimental observation reveal that the phonon-induced processes bridge the coupling between multiple degrees of freedom in the emitter-optomechanical interaction. This novel interaction greatly extends the cavity QED study and provides new paradigm to the quantum interface between spin defects, photons and phonons using atomically thin layered materials.

ACKNOWLEDGMENTS

All authors gratefully acknowledge the German Science Foundation (DFG) for financial support via grants FI 947/8-1, DI 2013/5-1, AS 310/9-1 and SPP-2244, as well as the clusters of excellence MCQST (EXS-2111) and e-conversion (EXS-2089). J. J. F. gratefully acknowledges the state of Bavaria via the One Munich Strategy and Munich Quantum Valley. C. Q. and V. V. gratefully acknowledge the Alexander v. Humboldt foundation for financial support in the framework of their fellowship programme. Support by the Ion Beam Center (IBC) at HZDR is gratefully acknowledged.

[1] T. T. Tran, K. Bray, M. J. Ford, M. Toth, and I. Aharonovich, Quantum emission from hexagonal boron

nitride monolayers, *Nat. Nanotechnol.* **11**, 37 (2016).

- [2] A. Sajid, M. J. Ford, and J. R. Reimers, Single-photon emitters in hexagonal boron nitride: a review of progress, *Rep. Prog. Phys.* **83**, 044501 (2020).
- [3] N. Mendelson, D. Chugh, J. R. Reimers, T. S. Cheng, A. Gottscholl, H. Long, C. J. Mellor, A. Zettl, V. Dyakonov, P. H. Beton, S. V. Novikov, C. Jagadish, H. H. Tan, M. J. Ford, M. Toth, C. Bradac, and I. Aharonovich, Identifying carbon as the source of visible single-photon emission from hexagonal boron nitride, *Nat. Mater.* **20**, 321 (2021).
- [4] H. L. Stern, Q. Gu, J. Jarman, S. Eizagirre Barker, N. Mendelson, D. Chugh, S. Schott, H. H. Tan, H. Sirringhaus, I. Aharonovich, and M. Atatüre, Room-temperature optically detected magnetic resonance of single defects in hexagonal boron nitride, *Nat. Commun.* **13**, 618 (2022).
- [5] M. Kianinia, S. White, J. E. Fröch, C. Bradac, and I. Aharonovich, Engineering spin defects in hexagonal boron nitride (2020), [arXiv:2004.07968](https://arxiv.org/abs/2004.07968).
- [6] A. Gottscholl, M. Kianinia, V. Soltamov, S. Orlinskii, G. Mamin, C. Bradac, C. Kasper, K. Krambrock, A. Sperlich, M. Toth, I. Aharonovich, and V. Dyakonov, Initialization and read-out of intrinsic spin defects in a van der waals crystal at room temperature, *Nat. Mater.* **19**, 540 (2020).
- [7] A. Gottscholl, M. Diez, V. Soltamov, C. Kasper, D. Krauß, A. Sperlich, M. Kianinia, C. Bradac, I. Aharonovich, and V. Dyakonov, Spin defects in hbn as promising temperature, pressure and magnetic field quantum sensors, *Nat. Commun.* **12**, 4480 (2021).
- [8] W. Liu, Z.-P. Li, Y.-Z. Yang, S. Yu, Y. Meng, Z.-A. Wang, Z.-C. Li, N.-J. Guo, F.-F. Yan, Q. Li, J.-F. Wang, J.-S. Xu, Y.-T. Wang, J.-S. Tang, C.-F. Li, and G.-C. Guo, Temperature-dependent energy-level shifts of spin defects in hexagonal boron nitride, *ACS Photonics* **8**, 1889 (2021).
- [9] V. Ivády, G. Barcza, G. Thiering, S. Li, H. Hamdi, J.-P. Chou, Ö. Legeza, and A. Gali, Ab initio theory of the negatively charged boron vacancy qubit in hexagonal boron nitride, *npj Comput. Mater* **6**, 41 (2020).
- [10] J. R. Reimers, J. Shen, M. Kianinia, C. Bradac, I. Aharonovich, M. J. Ford, and P. Piecuch, Photoluminescence, photophysics, and photochemistry of the V_B^- defect in hexagonal boron nitride, *Phys. Rev. B* **102**, 144105 (2020).
- [11] F. Libbi, P. M. M. C. de Melo, Z. Zanolli, M. J. Verstraete, and N. Marzari, Phonon-assisted luminescence in defect centers from many-body perturbation theory, *Phys. Rev. Lett.* **128**, 167401 (2022).
- [12] C. Qian, V. Villafañe, M. Schalk, G. V. Astakhov, U. Kentsch, M. Helm, P. Soubelet, N. P. Wilson, R. Rizzato, S. Mohr, A. W. Holleitner, D. B. Bucher, A. V. Stier, and J. J. Finley, Unveiling the zero-phonon line of the boron vacancy center by cavity-enhanced emission, *Nano Lett.* **22**, 5137 (2022).
- [13] S. Kim, J. E. Fröch, J. Christian, M. Straw, J. Bishop, D. Totonjian, K. Watanabe, T. Taniguchi, M. Toth, and I. Aharonovich, Photonic crystal cavities from hexagonal boron nitride, *Nat. Commun.* **9**, 2623 (2018).
- [14] J. E. Fröch, S. Kim, N. Mendelson, M. Kianinia, M. Toth, and I. Aharonovich, Coupling Hexagonal Boron Nitride Quantum Emitters to Photonic Crystal Cavities, *ACS Nano* **14**, 7085 (2020).
- [15] C. Qian, V. Villafañe, P. Soubelet, A. Hötger, T. Taniguchi, K. Watanabe, N. P. Wilson, A. V. Stier, A. W. Holleitner, and J. J. Finley, Nonlocal exciton-photon interactions in hybrid high- q beam nanocavities with encapsulated mos_2 monolayers, *Phys. Rev. Lett.* **128**, 237403 (2022).
- [16] N. Mendelson, M. Doherty, M. Toth, I. Aharonovich, and T. T. Tran, Strain engineering of quantum emitters in hexagonal boron nitride (2019), [arXiv:1911.08072](https://arxiv.org/abs/1911.08072).
- [17] M. Autore, P. Li, I. Dolado, F. J. Alfaro-Mozaz, R. Esteban, A. Atxabal, F. Casanova, L. E. Hueso, P. Alonso-González, J. Aizpurua, A. Y. Nikitin, S. Vélez, and R. Hillenbrand, Boron nitride nanoresonators for phonon-enhanced molecular vibrational spectroscopy at the strong coupling limit, *Light: Sci. Appl.* **7**, 17172 (2018).
- [18] Y. Wang, J. Lee, X.-Q. Zheng, Y. Xie, and P. X.-L. Feng, Hexagonal boron nitride phononic crystal waveguides, *ACS Photonics* **6**, 3225 (2019).
- [19] M. K. Zalalutdinov, J. T. Robinson, J. J. Fonseca, S. W. LaGasse, T. Pandey, L. R. Lindsay, T. L. Reinecke, D. M. Photiadis, J. C. Culbertson, C. D. Cress, and B. H. Houston, Acoustic cavities in 2d heterostructures, *Nat. Commun.* **12**, 3267 (2021).
- [20] S. Latini, U. De Giovannini, E. J. Sie, N. Gedik, H. Hübener, and A. Rubio, Phonoritons as Hybridized Exciton-Photon-Phonon Excitations in a Monolayer h -BN Optical Cavity, *Phys. Rev. Lett.* **126**, 227401 (2021).
- [21] T. Yang, N. Mendelson, C. Li, A. Gottscholl, J. Scott, M. Kianinia, V. Dyakonov, M. Toth, and I. Aharonovich, Spin defects in hexagonal boron nitride for strain sensing on nanopillar arrays, *Nanoscale* **14**, 5239 (2022).
- [22] M. Eichenfield, R. Camacho, J. Chan, K. J. Vahala, and O. Painter, A picogram- and nanometre-scale photonic-crystal optomechanical cavity, *Nature* **459**, 550 (2009).
- [23] M. Eichenfield, J. Chan, R. M. Camacho, K. J. Vahala, and O. Painter, Optomechanical crystals, *Nature* **462**, 78 (2009).
- [24] C. Qian, V. Villafañe, P. Soubelet, A. V. Stier, and J. J. Finley, Exciton coupling with cavity vibrational phonons and mos_2 lattice phonons in hybrid nanobeam cavities (2022), [arXiv:2204.04304](https://arxiv.org/abs/2204.04304).
- [25] M. Kianinia, S. White, J. E. Fröch, C. Bradac, and I. Aharonovich, Generation of spin defects in hexagonal boron nitride, *ACS Photonics* **7**, 2147 (2020).
- [26] N.-J. Guo, W. Liu, Z.-P. Li, Y.-Z. Yang, S. Yu, Y. Meng, Z.-A. Wang, X.-D. Zeng, F.-F. Yan, Q. Li, J.-F. Wang, J.-S. Xu, Y.-T. Wang, J.-S. Tang, C.-F. Li, and G.-C. Guo, Generation of spin defects by ion implantation in hexagonal boron nitride, *ACS Omega* **7**, 1733 (2022).
- [27] M. Aspelmeyer, T. J. Kippenberg, and F. Marquardt, Cavity optomechanics, *Rev. Mod. Phys.* **86**, 1391 (2014).
- [28] C. Dong, Y. Wang, and H. Wang, Optomechanical interfaces for hybrid quantum networks, *Natl. Sci. Rev.* **2**, 510 (2015).
- [29] J. Li, E. R. Glaser, C. Elias, G. Ye, D. Evans, L. Xue, S. Liu, G. Cassabois, B. Gil, P. Valvin, T. Pelinei, A. L. Yeats, R. He, B. Liu, and J. H. Edgar, Defect engineering of monoisotopic hexagonal boron nitride crystals via neutron transmutation doping, *Chem. Mater.* **33**, 9231 (2021).
- [30] J. Zhou, J. Zheng, Z. Fang, P. Xu, and A. Majumdar, Ultra-low mode volume on-substrate silicon nanobeam cavity, *Opt. Express* **27**, 30692 (2019).

- [31] J. Guo and S. Gröblacher, Integrated optical-readout of a high-q mechanical out-of-plane mode, *Light: Sci. Appl.* **11**, 282 (2022).
- [32] I. Wilson-Rae and A. Imamoglu, Quantum dot cavity-qed in the presence of strong electron-phonon interactions, *Phys. Rev. B* **65**, 235311 (2002).
- [33] G.-C. Shan, Z.-Q. Yin, C. H. Shek, and W. Huang, Single photon sources with single semiconductor quantum dots, *Front. of Phys.* **9**, 170 (2014).
- [34] R. Heitz, M. Veit, N. N. Ledentsov, A. Hoffmann, D. Bimberg, V. M. Ustinov, P. S. Kop'ev, and Z. I. Alferov, Energy relaxation by multiphonon processes in InAs/GaAs quantum dots, *Phys. Rev. B* **56**, 10435 (1997).
- [35] A. W. Achtstein, O. Marquardt, R. Scott, M. Ibrahim, T. Riedl, A. V. Prudnikau, A. Antanovich, N. Owschimikow, J. K. N. Lindner, M. Artemyev, and U. Woggon, Impact of shell growth on recombination dynamics and exciton-phonon interaction in CdSe-CdS core-shell nanoplatelets, *ACS Nano* **12**, 9476 (2018).
- [36] P. Merkl, C.-K. Yong, M. Liebich, I. Hofmeister, G. Berghäuser, E. Malic, and R. Huber, Proximity control of interlayer exciton-phonon hybridization in van der Waals heterostructures, *Nat. Commun.* **12**, 1719 (2021).
- [37] I. Iatsunskiy, G. Nowaczyk, S. Jurga, V. Fedorenko, M. Pavlenko, and V. Smytyna, One and two-phonon Raman scattering from nanostructured silicon, *Optik* **126**, 1650 (2015).
- [38] R. T. Howie, I. B. Magdău, A. F. Goncharov, G. J. Ackland, and E. Gregoryanz, Phonon localization by mass disorder in dense hydrogen-deuterium binary alloy, *Phys. Rev. Lett.* **113**, 175501 (2014).
- [39] A. K. Arora, M. Rajalakshmi, T. R. Ravindran, and V. Sivasubramanian, Raman spectroscopy of optical phonon confinement in nanostructured materials, *J. Raman Spectrosc.* **38**, 604 (2007).
- [40] V. I. Korepanov, Localized phonons in Raman spectra of nanoparticles and disordered media, *J. Raman Spectrosc.* **51**, 881 (2020).
- [41] G. Grosso, H. Moon, C. J. Ciccarino, J. Flick, N. Mendelson, L. Mennel, M. Toth, I. Aharonovich, P. Narang, and D. R. Englund, Low-temperature electron-phonon interaction of quantum emitters in hexagonal boron nitride, *ACS Photonics* **7**, 1410 (2020).
- [42] D. Hoch, X. Yao, and M. Poot, Geometric tuning of stress in pre-displaced silicon nitride resonators, *Nano Lett.* **22**, 4013 (2022).
- [43] P. Wang, W. Chen, F. Wan, J. Wang, and J. Hu, A review of cavity-enhanced Raman spectroscopy as a gas sensing method, *Appl. Spectrosc. Rev.* **55**, 393 (2020).
- [44] H. Xie, S. Jiang, D. A. Rhodes, J. C. Hone, J. Shan, and K. F. Mak, Tunable exciton-optomechanical coupling in suspended monolayer MoS₂, *Nano Lett.* **21**, 2538 (2021).
- [45] M. Montinaro, G. Wüst, M. Munsch, Y. Fontana, E. Russo-Averchi, M. Heiss, A. Fontcuberta i Morral, R. J. Warburton, and M. Poggio, Quantum dot optomechanics in a fully self-assembled nanowire, *Nano Lett.* **14**, 4454 (2014).

Supplemental Material for Active Cavity Optomechanics Based on Phonon-Induced Light-Matter Interactions

Chenjiang Qian,^{1,*} Viviana Villafañe,¹ Martin Schalk,¹ Georgy V. Astakhov,² Ulrich Kentsch,² Manfred Helm,² Pedro Soubelet,¹ Andreas V. Stier,¹ and Jonathan J. Finley^{1,†}

¹Walter Schottky Institut and Physik Department,

Technische Universität München, Am Coulombwall 4, 85748 Garching, Germany

²Helmholtz-Zentrum Dresden-Rossendorf, Institute of Ion Beam Physics and Materials Research, 01328 Dresden, Germany

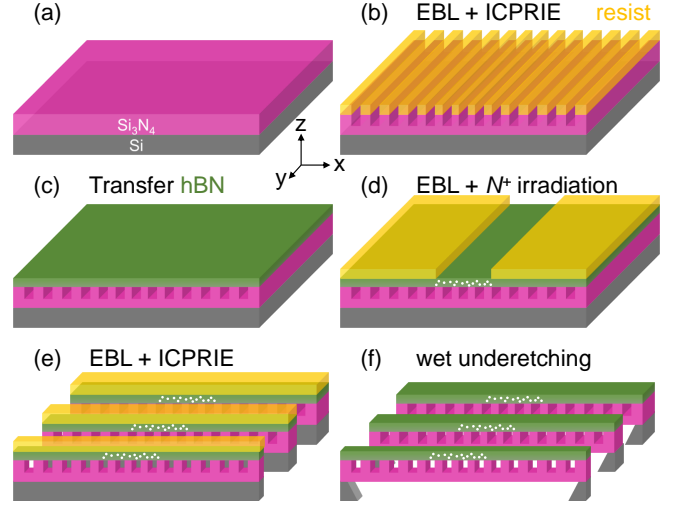
CONTENTS

I. General Methods	1
A. Sample Fabrication	1
B. Measurement Setup	2
C. Fitting Methods	2
II. Emitter-Induced Optomechanics	4
A. Control Experiments	4
B. Photon-Phonon Coupling	4
C. Power Dependence	4
D. Master Equation Theory	5
III. Optomechanical-Induced Control of V_B^- Emission and Phonons	6
A. Control Experiments and Raman Identification	6
B. Generality and Accuracy in Position Dependence	7
C. Anticrossing between V_B^- Phonons	8
D. Superposition of Cavity Vibronic Modes	9
E. Other Minor Effects of V_B^- Phonons	11
IV. Resonant Excitation: Methods and Control Experiments	12
V. Additional Discussions	12
References	12

I. GENERAL METHODS

A. Sample Fabrication

The hBN/Si₃N₄ hybrid nanobeam cavity is fabricated through e-beam lithography (EBL), inductively coupled plasma reactive ion etching (ICPRIE), viscoelastic dry transfer method [1] and wet underetching. Fabrication procedures of Sample-A are schematically depicted in SFig. 1. Firstly, we prepare Si substrate with 200nm Si₃N₄ grown by low pressure chemical vapor deposition (LPCVD) on top as shown in SFig. 1(a). Then we use



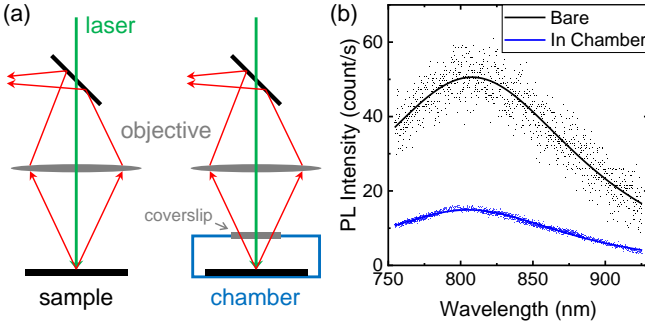
SFig. 1. Fabrication procedures. (a) Si₃N₄/Si substrate. (b) EBL and ICPRIE to fabricate periodic nanotrenches. (c) Transfer the hBN flake on top of the nanotrenches. (d) Generate V_B^- site-selectively. (e) EBL and ICPRIE to divide the nanobeams. (f) Wet underetching to remove the bottom Si.

EBL and ICPRIE to etch periodic nanotrenches in Si₃N₄, as shown in SFig. 1(b). We chirp the periodicity of nanotrenches at the center to create photonic bandgap confinement. After removing the residual resist, we transfer the hBN flake with a thickness ~ 100 nm on top of the nanotrenches, as shown in SFig. 1(c). We coat the hBN flake by the resist mask and use EBL to pattern a window at the cavity center, followed by the ion irradiation to create V_B^- centers through the window, as shown in SFig. 1(d). In this step the resist has the thickness > 600 nm to protect the under lying hBN [2]. Finally, we use EBL and ICPRIE to divide the nanobeams, as shown in SFig. 1(e), followed by a wet underetching to remove the bottom Si, as shown in SFig. 1(f). The fabrication procedures of Sample-B are generally the same. The only difference is that the V_B^- centers in Sample-B are not created site-selectively, but rather homogeneously in the whole hBN flake (without any resist mask) after all other fabrication procedures.

As shown in SFig. 1, the hBN in our cavity is not perforated by the periodic nanotrenches and only etched at two sidewalls of the nanobeam. This novel structure retains the *pristine* 2D semiconductors and improves the Q-factor to $\sim 10^5$, at least one order of magnitude higher

* chenjiang.qian@wsi.tum.de

† finley@wsi.tum.de



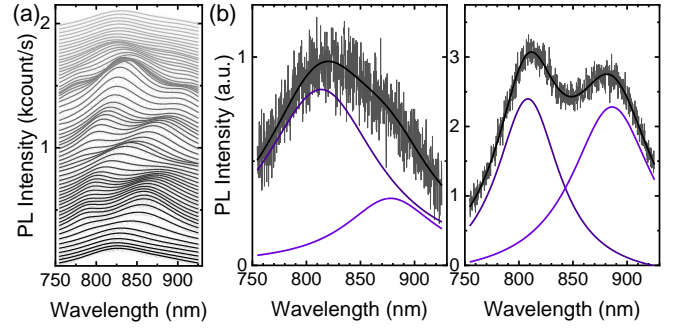
SFig. 2. (a) Schematic of the confocal micro-PL setup, with the sample (left) bare in the air and (right) in the chamber. (b) Comparison of PL spectra of V_B^- in bare (black) and in the chamber (blue), recorded at the same position with the same laser power of $264 \mu\text{W}$.

compared to conventional 2D-material nanocavities using the pick-and-place method or perforated hBN flakes. Detailed parameters used in fabrication and the calculation of cavity photonic modes have been reported in our previous works [3–5].

B. Measurement Setup

Photoluminescence (PL) and Raman spectroscopy in this work are recorded using a confocal micro-PL setup. The objective with a magnification of 100 and a NA of 0.75 is used to focus the laser into a spot with the size $\sim 1 \mu\text{m}^2$ on the sample. The resonant excitation of cavity photons (Fig. 4) is carried out with a tunable narrow-band cw-laser. Other experiments are carried out with a 532nm cw-laser. The samples are mounted on a three-dimensional xyz nanopositioner for the spatially resolved spectroscopy. The PL and Raman spectra of V_B^- centers (Fig. 2-4) are collected by a matrix array Si CCD detector in a spectrometer, with the focal length of 0.55 m and the grating of 300 grooves per mm. The PL spectra of cavity photons (Fig. 1) are collected by the same detector and spectrometer but with the grating of 1200 grooves per mm.

In this work, the sample is measured at room temperature bare in the air, since we find that the coverslip of our chamber will suppress and deform the signals, particularly at long wavelength over 800 nm. The confocal setup is schematically depicted in SFig. 2(a). For a high NA objective, the medium lying coverslip will critically degrade the aplanatic and sine conditions, thereby introduces the spherical and chromatic aberrations [6, 7]. As a result, we observe a suppression of signals when the sample is measured in the chamber e.g., the comparison presented in SFig. 2(b). Moreover, we find this suppression increases with the photon wavelength, by $\sim 25\%$ from 800 to 920 nm. For PL signal of a sharp peak, such suppression will only decrease the counts and rarely affect the lineshape. However, for the broad V_B^- emission,



SFig. 3. (a) Example of PL spectra at different positions. Peaks are clearly distinguished. (b) Two examples of multi Lorentz fitting.

the lineshape will be distorted by the non-uniform suppression. Therefore, we measure the sample bare in the air to collect the pure signals and avoid potential errors.

C. Fitting Methods

The PL peaks are clearly distinguishable. Indeed, the shifting of peaks can be observed and traced even without fittings e.g., the spectra in Fig. 3 and SFig. 3(a) here. Nevertheless, we use multi Lorentz fittings to improve the accuracy of extracted data. Two examples are presented in SFig. 3(b). As shown, the fitting results are in good agreement with the raw data.

In this work, we fit the PL spectra in wavelength dimension for accuracy. The PL spectra are defined by the energy density distribution, as

$$\Delta E = f(\lambda) \Delta\lambda = g(\omega) \Delta\omega \quad (1)$$

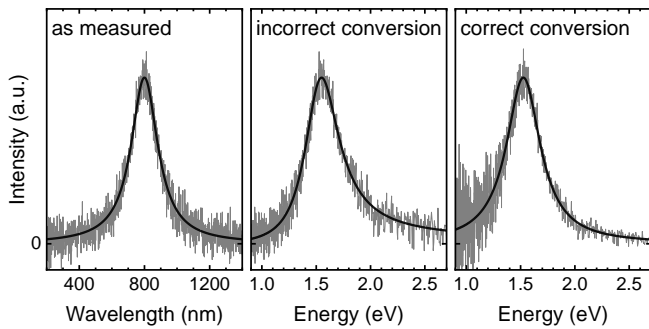
, where ΔE is the energy of photons in the differential wavelength range $\Delta\lambda$ or energy range $\Delta\omega$. The raw data collected by the spectrometer is $f(\lambda)$ at the wavelength λ dimension with equispaced points which means a constant $\Delta\lambda$. When converting the spectrum to the energy ω dimension, theoretically we cannot simply change the x-axis unit since $g(\omega) \neq f(\hbar c_0/\omega)$ but

$$\begin{aligned} g(\omega) &= f(\lambda) \frac{\Delta\lambda}{\Delta\omega} \\ &= f\left(\frac{\hbar c_0}{\omega}\right) \frac{\hbar c_0}{\omega^2} \end{aligned} \quad (2)$$

, where h is the Planck constant and c_0 is the vacuum light speed. For example, after converting the standard Lorentz peak with intensity A , peak wavelength λ_C and linewidth γ_λ

$$f(\lambda) = \frac{A}{\pi} \frac{\gamma_\lambda/2}{(\lambda - \lambda_C)^2 + (\gamma_\lambda/2)^2} \quad (3)$$

by Eq. (2), the spectra in the energy dimension still has



SFig. 4. Comparison of the spectra as measured, incorrectly converted, and correctly converted. Black line is the standard Lorentz signal. Gray line is the presumption of collected data by adding a normal distributed noise.

the standard Lorentz shape

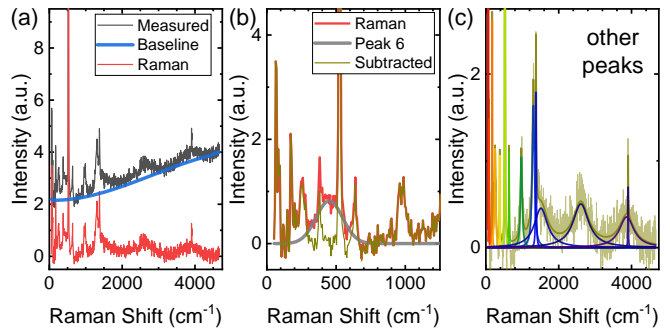
$$g(\omega) = \frac{A}{\pi} \frac{\gamma\lambda/2}{(hc_0/\omega - \lambda_c)^2 + (\gamma\lambda/2)^2} \frac{hc_0}{\omega^2} = \frac{A}{\pi} \frac{\gamma\omega/2}{(\omega - \omega_c)^2 + (\gamma\omega/2)^2} \quad (4)$$

with the peak energy ω_c and linewidth $\gamma\omega$ as

$$\begin{aligned} \omega_c &= \frac{hc_0}{\lambda_c} \frac{1}{1 + \beta^2} \\ \gamma\omega &= \frac{hc_0\gamma\lambda}{\lambda_c^2} \frac{1}{1 + \beta^2} \\ \beta &= \frac{\gamma\lambda}{2\lambda_c} = \frac{\gamma\omega}{2\omega_c} \end{aligned} \quad (5)$$

. In contrast, if we simply convert the x-axis unit without the term $\Delta\lambda/\Delta\omega$ in Eq. (2), the incorrect result $f(hc_0/\omega)$ will lose the Lorentz shape.

However, the conversion in Eq. (2) is only theoretically feasible, limited by the experimental noises. To straightforwardly clarify this point, we plot one example of the Lorentz signal with $\lambda_c = 800$ nm and $\gamma\lambda = 200$ nm in SFig. 4. We add a noise following the normal distribution to simulate experimental fluctuations, and the presumptive data in measurement is depicted by the gray line. As shown, after the incorrect conversion without the term $\Delta\lambda/\Delta\omega$, the peak in the energy dimension is deformed and not Lorentzian. Although the correct conversion by Eq. (2) retains the Lorentz lineshape in the energy dimension, the noise of data point significantly increases at low ω side. Such non-uniform noise of data points makes the further analysis difficult. Generally, for a narrow PL peak either the incorrect or correct conversion (without or with $\Delta\lambda/\Delta\omega$) works, because $\Delta\lambda/\Delta\omega$ is approximately constant within the narrow range. But for broad PL peaks, the inaccurate deformation in incorrect conversion and the non-uniform noise in correct conversion both increase as the peak linewidth becomes broader (larger β in Eq. (5)), thus are both infeasible. Therefore, we use multi Lorentz peaks to fit the broad V_B^- emission in wavelength dimension (e.g. SFig. 3), and

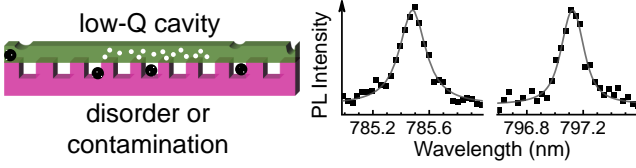


SFig. 5. (a) Raman spectrum (red) is extracted by subtracting the measured spectrum (gray) with the emission baseline (blue). (b) Peak 6 overlaps to many other peaks. Thereby, we first subtract the Raman spectrum with a Gaussian-shape peak 6 (gray). (c) Other Raman peaks (color lines) are then extracted by the multi Lorentz fitting.

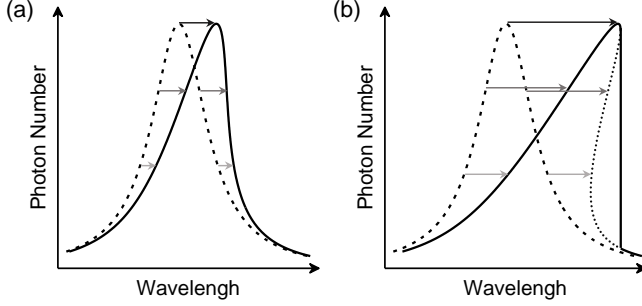
convert the fitting peak wavelengths to energy dimension when necessary.

Above discussions are based on the theoretical definition of spectrum Eq. (1) and the correct collection of $f(\lambda)$ by the spectrometer. One might wonder that the actual performance of spectrometer might differ to the expectation, e.g. Si CCD detector usually has low efficiency for the wavelength over 1000 nm, limiting the accuracy of Eq. (1). We mainly focus on the spectra with wavelength < 950 nm to avoid the inaccuracy from Si CCD detector. In addition, we note that the PL peak shifts such as those shown in SFig. 3 are very distinguishable. Even if some inaccuracies are introduced by the fitting, they will not affect the conclusions.

The recorded spectra around the wavelength of excitation laser, such as the gray line in SFig. 5(a), consist of Raman and PL signals superimposed. As a common method, we first draw the emission baseline based on the peak foots of Raman signals, and then extract the Raman spectrum by subtracting the emission baseline from the recorded data, such as the example in SFig. 5(a). In the Raman spectra, the broad peak 6 of highly localized phonon overlaps with many other peaks. Thereby, it is difficult to fit all overlapped peaks together. To separate these peaks, we first extract peak 6 by a Gaussian base peak as shown in SFig. 5(b). Then other peaks are fitted by multi Lorentz peaks as shown in SFig. 5(c). This fitting method might introduce a bit inaccuracy of peak 6. However, as shown in Fig. 2(c) and SFig. 5(b) here, peak 6 and other nearby peaks are quite distinguishable, thereby the inaccuracy is small. Moreover, as discussed in the main paper, the V_B^- emission wavelengths mainly depend on multi-phonon states of highly localized phonons represented by peak 12 and 13. Thus, even if some minor inaccuracy exists in the fitting of peak 6, our analysis will not be affected. In addition, we note that for the broad peaks of highly localized phonons in $1400-4000$ cm^{-1} , such as the three in SFig. 5(c), Lorentz and Gaussian fittings give the same peak energies since



SFig. 6. Asymmetry is not observed in irradiated but low-Q (< 7000) cavities.



SFig. 7. Brief theory. The peak of cavity photon is symmetric (dashed line) without phonon but asymmetric (solid line) due to a non-uniform shift (arrows) arising from the photon-phonon coupling e.g., with the (a) small or (b) large shift.

these peaks are distinguishable and do not overlap with other peaks. Therefore, the inaccuracy from the fitting methods of PL and Raman spectra has little impact on the conclusions in this work.

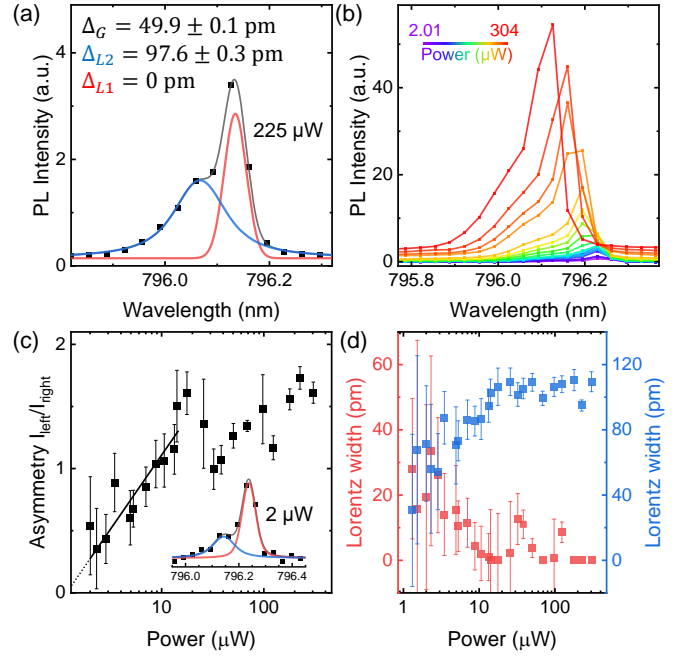
II. EMITTER-INDUCED OPTOMECHANICS

A. Control Experiments

We emphasize that we observe the asymmetric lineshape for high-Q ($> 10^4$) cavity photonic modes. However, the fabrication procedures sometimes introduce disorder or contamination into the hBN/Si₃N₄ nanobeam, which limit the cavity photonic mode to low-Q regime as schematically shown in SFig. 6. As a result, we do not observe the asymmetric peak for the cavity photonic modes with Q-factor smaller than 7000. This is due to that photon-phonon coupling effects strongly rely on the Q-factor (decay rate of cavity photons), as discussed in next Sec. II B.

B. Photon-Phonon Coupling

The asymmetric of cavity emission lineshape is a typical phenomenon arising from photon-phonon couplings [8–10], which can be explained by a simple theory shown in SFig. 7. Without the photon-phonon coupling, the spectral density of cavity photons is well described by a



SFig. 8. (a) The bi-Voigt fitting of the PL peak of cavity photons. (b) The power-dependent PL spectra. (c) The ratio between the intensity of two Voigt peaks, as a quantitation of the asymmetry. (d) The Lorentz width of the Voigt peaks, as a quantitation of the perpendicularity of the lineshape.

Lorentz lineshape given by

$$\pi D_C(\omega) = (\gamma_a/2)/[(\omega - \omega_a)^2 + (\gamma_a/2)^2] \quad (6)$$

where ω_a and γ_a are the energy and linewidth (decay rate) of cavity photons [11]. Considering the photon-phonon coupling with the phonon energy ω_q and the coupling strength λ_{p-q} to a single photon, the optical resonance will be red shifted by an amount of $8\lambda_{p-q}^2 N(\omega)/\omega_q$. $N(\omega)$ is the photon population proportional to $D_C(\omega)$. Therefore, as shown in SFig. 7(a)(b), more photons at the peak energy result in larger redshift arising from the photon-phonon coupling. This non-uniform energy shift results in the asymmetric peak lineshape. Moreover, when the total population of photons N larger than the threshold value as [8–10]

$$N > \frac{\omega_q \gamma_a}{6\sqrt{3}\lambda_{p-q}^2} \quad (7)$$

the peak is strongly deformed with a nearly perpendicular line shape at long wavelength side, such as shown in SFig. 7(b).

C. Power Dependence

Generally, as the excitation laser power increases, the asymmetry in the lineshape of cavity photons will increase since the photon-phonon coupling increases with

the population of photons and phonons. For passive cavity without emitters, the peak wavelength should continuously red shift as the photon-phonon coupling increases [9, 10]. However, in our active cavities with V_B^- centers, the situation is complex. Firstly, the PL spectrum is broadened by our measurement setup following the convolution to a Gaussian window function [12, 13]. This broadening decreases the resolution and distinguishability of the PL spectra, as shown in SFig. 8(a). Secondly, in active cavities there exist multiple factors contributing to the power-dependent shift of cavity resonance, e.g., the laser-induced oxidation of emitters [14] and the pump-induced dephasing of cavity-emitter coupling [12, 15]. Thus, the peak wavelength will not simply red shift as observed for passive cavities. Indeed, blue shift is observed in our cavities with the increasing power, as shown in SFig. 8(b).

Despite these limitations, we still observe the photon-phonon coupling increasing with the laser power. We use two Voigt peaks [12], which is the convolution of Lorentz and Gaussian peak, to fit the PL peak of cavity photons as presented in SFig. 8(a). We note that such two peaks have no general physical meanings but provide a quantitation to describe the asymmetry and perpendicularity of the lineshape. The Gaussian width is set the same for the two Voigt peaks, and the fitting result in SFig. 8(a) shows this width $\Delta_G = 49.9 \pm 0.1$ pm, consistent to the resolution 50 pm of our spectrometer. Thereby, we fix $\Delta_G = 50$ pm in the fitting of other PL peaks. We use the ratio between the intensity of two Voigt peaks as the quantitation of asymmetry, and the results are presented in SFig. 8(c). As shown, the asymmetry generally increases with the laser power, and indicates a threshold power for the asymmetric lineshape of 9 ± 2 μ W. In addition, the Lorentz width Δ_L of Voigt peak describes the actual lineshape before broadened by the spectrometer. Smaller Δ_L means more perpendicular lineshape. The Lorentz width of two Voigt peaks are presented in SFig. 8(d). As shown, when the power exceeds a threshold value of 10 μ W, Δ_L of the right peak (red) becomes zero, corresponding to the nearly perpendicular lineshape in SFig. 7(b). These results in SFig. 8 clearly reveal the photon-phonon coupling increases with the laser power.

D. Master Equation Theory

The simple theory in Sec. II B shows that the optomechanical coupling (asymmetry) increases with the laser power, but does not discuss the originality of phonons in the coupling. In the main paper, we present the phonon-induced light-matter coupling model to explain the V_B^- -induced photon-phonon coupling. Here we present this theory in detail.

Since specific dynamic and parameters of the phonon-induced processes during the V_B^- emission are not fully known yet [16–18], we consider a brief system consisting of a single emitter described by the ground state G and

the excited state X with the energy ω_X and decay rate γ_X , a single cavity photonic mode with the energy ω_a and decay rate γ_a , and a single phonon mode with the energy ω_q and decay rate γ_q . The Hamiltonian of the cavity QED system is thereby wrote as

$$H = H_e + H_p + H_q + H_{e-q} + H_{p-q} + H_{e-p} \quad (8)$$

involving the 6 terms correspond to emitter (H_e), photon (H_p), phonon (H_q), emitter-phonon coupling (H_{e-q}), photon-phonon coupling (H_{p-q}), emitter-photon coupling (H_{e-p}), respectively. The first three terms are clearly defined as

$$\begin{aligned} H_e &= \hbar\omega_X \sigma_{X,X}, \\ H_p &= \hbar\omega_a a^\dagger a \\ H_q &= \hbar\omega_q q^\dagger q \end{aligned} \quad (9)$$

where $\sigma_{A,B} = |A\rangle\langle B|$ ($A, B \in \{X, G\}$) is the Dirac operator for the emitter, a^\dagger/a are the ladder operators for photons in the cavity photonic mode, and q^\dagger/q are the ladder operators for phonons. For an atomic V_B^- defect, the oscillatory motion of confined electron is expected to be much faster than the phonon frequency (adiabatic approximation) [19], thereby, the two phonon coupling terms are wrote as

$$\begin{aligned} H_{e-q} &= \hbar\lambda_{e-q} \sigma_{X,X} (q + q^\dagger) \\ H_{p-q} &= \hbar\lambda_{p-q} a^\dagger a (q + q^\dagger) \end{aligned} \quad (10)$$

where λ_{e-q} and λ_{p-q} are the strength for emitter-phonon and photon-phonon coupling, respectively. The emitter-photon coupling with a strength g is usually described by the Jaynes-Cummings model as

$$H_{e-p} = \hbar g (\sigma_{G,X} a^\dagger + \sigma_{X,G} a) \quad (11)$$

which means the $X \rightarrow G$ transition emit a photon to the cavity photonic mode, and a photon in the cavity photonic mode excite the emitter as $G \rightarrow X$. However, the V_B^- emission is dominated by the phonon-induced processes. Hereby we introduce an effective phonon-induced emitter-photon coupling, e.g.,

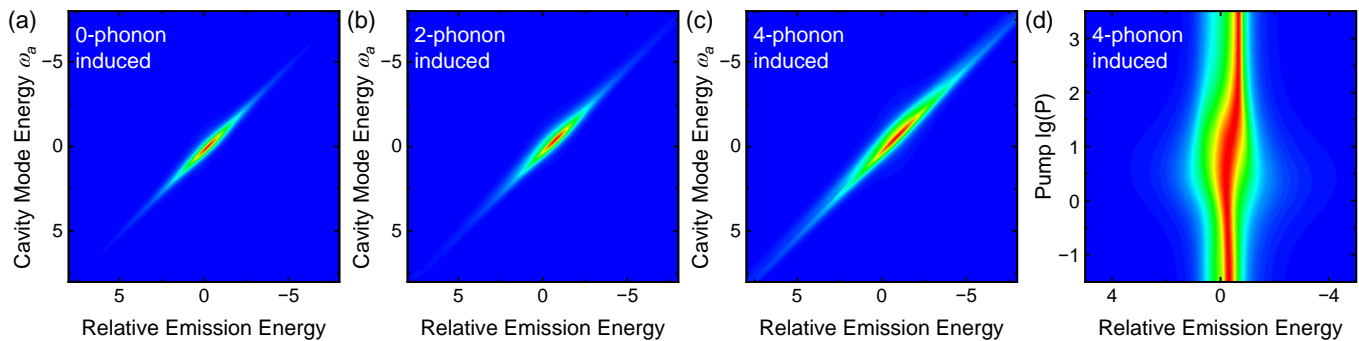
$$H_{e-p} = \hbar g (\sigma_{G,X} q^\dagger a^\dagger + \sigma_{X,G} q a) \quad (12)$$

for one-phonon-induced emitter-photon coupling and

$$H_{e-p} = \hbar g (\sigma_{G,X} (q^\dagger)^k a^\dagger + \sigma_{X,G} q^k a) \quad (13)$$

for k -phonon-induced emitter-photon coupling.

We emphasize that, Eq. (11) corresponds to the conventional case, where the phonon couplings in Eq. (10) introduces vibronic sublevels which *mediate* the emitter-photon coupling. In contrast, Eq. (12) or (13) is totally different, which means the phonon is necessary to *induce* the emitter-photon coupling. We next present and compare the calculation result between usual emitters (dominated by zero-phonon line) represented by Eq. (11) and V_B^- represented by Eq. (13).



SFig. 9. Emission spectra from the cavity photonic mode, calculated with the emitter-photon coupling induced by (a) none, (b) two, and (c) four phonons. The asymmetric lineshape arising from the photon-phonon coupling is clearly observed with the phonon-induced couplings in (b)(c). (d) Normalized pump-dependent spectra. As the pump increases, the narrowing of the emission peak at low energy side agrees well to the experimental results in SFig. 8(d).

The steady state of the cavity QED system is calculated by solving the master equation

$$\frac{d}{dt}\rho = -\frac{i}{\hbar}[H, \rho] + \sum_n \mathcal{L}(c_n) \quad (14)$$

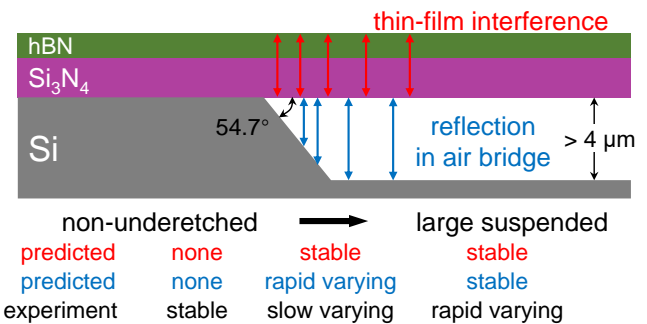
where ρ is the density matrix of the system states. Here we consider the system states with one photon and seven phonons allowed at maximum. H is Hamiltonian defined in Eq. (8), and here we calculate the three cases corresponding to the emitter-photon coupling described by Eq. (13) with $k = 0, 2, 4$, respectively. $k = 0$ is equal to Eq. (11). The Liouvillian superoperator

$$\mathcal{L}(c_n) = 1/2 (2c_n\rho c_n^\dagger - \rho c_n^\dagger c_n - c_n^\dagger c_n\rho) \quad (15)$$

$$c_n = \{\sqrt{\gamma_X}\sigma_{G,X}, \sqrt{\gamma_a}a, \sqrt{\gamma_q}q, \sqrt{P}\sigma_{X,G}\}$$

describes Markovian processes corresponding to the decay of emitter, decay of photon, decay of phonon, and pump of emitter with the rate P , respectively. Here we use $\omega_X = 0$, $\omega_q = 0.2$, $\lambda_{e-q} = 0.4$, $\lambda_{p-q} = 0.2$, $g = 0.1$, $\gamma_X = 2$, $\gamma_a = 0.2$, $\gamma_q = 0.2$, $P = 0.002$, and a sweeping $\omega_a \in (-10, 10)$ to calculate the emission from the cavity photonic mode. For brevity, we omit the energy unit meV for the parameters and set $\hbar = 1$. The spectra in the three cases are presented in SFig. 9(a)-(c) (also in Fig. 1(b)) exhibiting an obvious comparison. For the conventional H_{e-p} , the asymmetry in the emission lineshape is limited. In contrast, the asymmetry is clearly observed for the two-phonon induced coupling and even stronger in the four-phonon case. We also calculate the pump-dependent emission with $\omega_a = 0$, and present the normalized spectra in SFig. 9(d). As the pump increases, the emission peak becomes narrower at the low energy (long wavelength) side, consistent to the experimental results in SFig. 8(d).

We note that, we use the brief system and parameters around the reference magnitudes [4, 8] for a qualitative description of the phonon-induced processes of V_B^- emission. The actual case could be complex involving multiple phonon modes and many-body effects. Further simulation is limited by the fact that the specific details of



SFig. 10. Excluding air-bridge reflection and thin-film interference. As shown, the predicted position dependence of two effects in freely suspended structures can neither match the experimental observations.

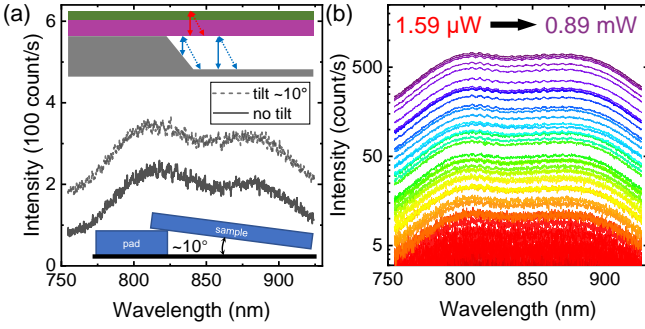
V_B^- emission remain unknown yet [16–18]. Nonetheless, our brief model already clearly shows how the phonon-induced processes result in the photon-phonon (optomechanical) coupling phenomena, thereby, well explains our experimental observations.

III. OPTOMECHANICAL-INDUCED CONTROL OF V_B^- EMISSION AND PHONONS

A. Control Experiments and Raman Identification

The position and geometry dependence in the PL and Raman spectra of V_B^- centers are well explained by the vibronic modes. Hereby, we first present control experiments and discussions to exclude other possible factors.

As shown in SFig. 10, the reflection in the underetched air bridge and the thin-film interference are two possible factors which might affect the PL spectra. The air bridge in sample-B is etched with 50% KOH solution, exhibiting a strong anisotropic etching that means (111) surface of Si cannot be etched. Thus, the etching angle at the boundary of Si is always 54.7° as denoted in

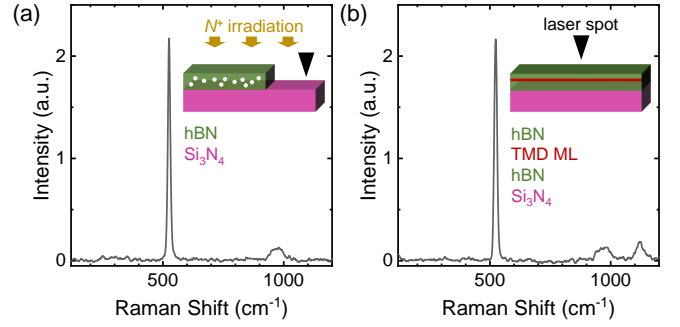


SFig. 11. (a) Comparison of PL spectra by tilting the sample. Little difference is observed. (b) Power-dependent PL spectra. No shifting or merging of peaks is observed.

SFig. 10. If the optical reflections in the air bridge plays the major role, their effect should vary rapidly at the boundary while be stable away the boundary. The thin-film interference depends on the thickness of hBN and Si_3N_4 , which have little variation in the whole sample. Therefore, the position dependence of these two effects can be predicted, as denoted in SFig. 10. However, as presented in Fig. 3, the position-dependent PL and Raman spectra vary slowly at the boundary while rapidly away from the boundary. The prediction of two effects can neither match the experimental observations in the large suspended membrane. Indeed, due to the high-concentration KOH solution used in the wet underetching, undissolved residuals left at the bottom surface of air bridge as shown in Fig. 2(b). With such rough surface, the reflection effect in the air bridge is expected to be neglectable.

In addition, the air bridge reflection and thin-film interference strongly depend on the tilting of the sample, as shown by the solid (before tilting) and dashed (after tilting) arrows in the inset of SFig. 11(a). Particularly, the air bridge reflection should exhibit huge differences around the boundary, due to the 54.7° etching surface of Si. However, little difference is observed after we tilt the sample $\sim 10^\circ$. The PL spectra measured at a same position before (solid) and after (dash) tilting are shown in SFig. 11(a) for example. Meanwhile, if the multi PL peaks and anticrossings we observed are from the thin-film interference or other optical effects, we should observe peak shifts as the optical coupling dephased by the increasing laser power [12, 15]. However, no shift is observed as shown in the power-dependent PL spectra in SFig. 11(b). Considering the obvious contradictions between predictions and experimental results presented in SFig. 10 and 11, we exclude the optical effects of air-bridge reflection and thin-film interference from our experimental observations.

We also carry out control experiments to identify the Raman peaks. A Raman spectrum recorded at irradiated Si_3N_4 substrate without hBN is plotted in SFig. 12(a). Only peaks 7 and 9 from bulk Si_3N_4 are observed, indicating that even if some defects in Si_3N_4 are created in



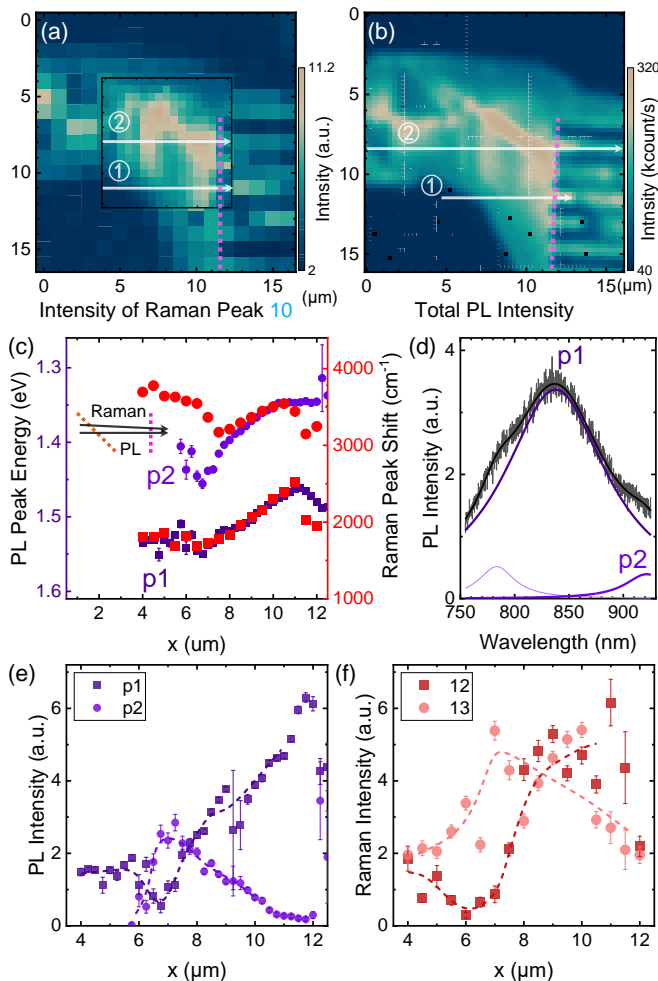
SFig. 12. (a) Raman spectrum recorded at Si_3N_4 substrate after N^+ ion irradiation (no hBN). (b) Raman spectrum recorded at hBN/MoS₂/hBN heterostructure on Si_3N_4 substrate, without irradiation. Both are excited by 532nm cw-laser.

irradiation, they generate few Raman signals in our measurement range. In SFig. 12(b) we plot a Raman spectrum recorded from hBN/MoS₂/hBN/ Si_3N_4 nanobeam without irradiation [5]. Other peaks that have not been observed in these control experiments are thereby identified from V_B^- related phonons.

B. Generality and Accuracy in Position Dependence

In our measurement, the PL and Raman spectra are recorded separately. Typical Raman and PL map are presented in SFig. 13(a)(b), respectively. As shown, the intensity of Raman peak 10 in (a) generally follows the total PL intensity in (b). This correspondence is due to that, independent of whether the emission arises from one phonon replica or the other, the total PL intensity is determined by the emitters excited through the trapping process (blue dashed arrow in Fig. 2(a)) in which phonon mode represented by Raman peak 10 dominates. A similar correspondence between the intensity of a specific phonon mode and the integrated total PL intensity has been observed for nitrogen vacancies in hBN [20], further supporting that phonon mode 10 is involved in the excitation of V_B^- . In addition to the correspondence between the energy of highly localized phonons and the wavelengths of V_B^- emission peaks, our experimental results perfectly agree with the picture of two phonon processes in the V_B^- emission in Fig. 2(a).

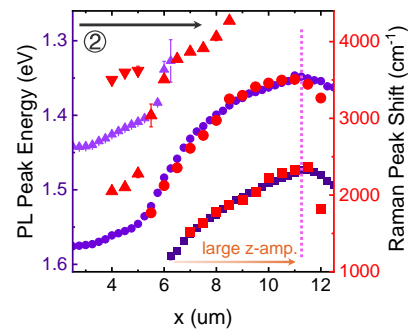
We note that the accuracy of the comparison between PL and Raman spectra is limited by the misalignments between the two maps, which introduce some minor mismatch in the results e.g., in SFig. 13(c) we plot the energies of PL and Raman peaks corresponding to Fig. 3. There are mainly two misalignments. Firstly, as presented in SFig. 13(a)(b), the two maps have a small relative angle. Secondly, the integration time for each Raman spectrum is at least 10 times of that for each PL spectrum, thereby, we need to decrease the resolution of the



SFig. 13. Intensity map of (a) extended phonon peak 10 and (b) total PL emission. (c) Energies of PL and Raman peaks extracted from trace ① in (a)(b), corresponding to Fig. 3(a)(b). Inset depicts potential misalignments between the trace in the two maps. The orange and magenta dashed lines correspond to the boundaries between different regions. (d) Fitting of PL spectrum at $x = 12 \mu\text{m}$. Fitting of p1 is accurate while that of p2 is limited by the measurement. (e) Extracted intensities of PL peaks and (f) Raman peaks. PL peak p1 quantitatively tracks Raman peak 12 whilst PL peak p2 qualitatively tracks Raman peak 13.

Raman map for feasibility. As shown in SFig. 13(a), we first use the step of $1 \mu\text{m}$ for a large $16 \times 16 \mu\text{m}$ Raman map, and then use the step of $0.5 \mu\text{m}$ for a small $8 \times 8 \mu\text{m}$ Raman map. In contrast, we use the step of $0.25 \mu\text{m}$ for the PL map in SFig. 13(b). The different resolution means an unavoidable translational misalignment. These two misalignments are schematically depicted in the inset in SFig. 13(c).

Meanwhile, the fitting accuracy of PL peaks at long wavelength is limited by the measurement. Indeed, datasets in Fig. 3(a)-(b) are exactly extracted from the trace ① in SFig. 13(a)(b). The PL spectrum at $x = 12 \mu\text{m}$ in SFig. 13(c) is presented in (d) along with the



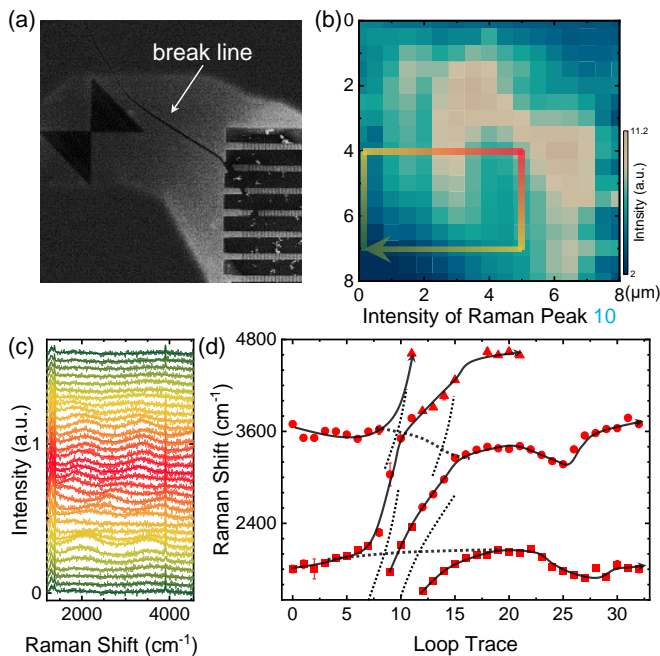
SFig. 14. Energy of PL peaks and highly localized phonons extracted from trace ② in SFig. 13(a)(b).

multi Lorentz fitting. As shown, the fitting of PL peak p1 is accurate, but the fitting accuracy of p2 is limited since part of peak p2 is outside the measurement range. We note that even if we increase the measurement range, e.g., installing a grating of 150 grooves per mm, the fitting accuracy at long wavelength will still be limited by the low efficiency of Si CCD detector at long wavelength. Thus, as shown in SFig. 13(c), the fitting energy of PL peak p1 quantitatively tracks the shift of corresponding highly localized phonon, whilst that of p2 qualitatively tracks. The corresponding intensity of PL and Raman peaks are plotted in SFig. 13(e)(f). Similarly, the intensity of PL peak p1 agrees quantitatively to that of Raman peak 12, while the intensity of p2 qualitatively agrees to that of Raman peak 13. This is why we mainly focus on the PL peak p1 when later discussing the superposition of vibronic modes in SFig. 18 in Sec. III D.

The consistence between PL and Raman spectra arising from the two phonon processes in Fig. 2(a) is generally observed in our measurement. The generality of the agreement between the intensity of Raman peak 10 and total PL intensity, which corresponds to the trapping process, is already shown by the comparison of SFig. 13(a)(b). In SFig. 14 we plot the shifts of highly localized phonons and PL peaks extracted from trace ② in SFig. 13(a)(b). Compared to trace ①, the amplitude of z-vibrations in trace ② is much larger since the positions are far away from the non-underetched region. As a result, the total PL intensity exhibits an eight-fold enhancement at the position having maximum z-amplitude, compared to the non-underetched region [21]. Moreover, the good agreement between the PL and Raman peak shifts is again observed, except minor mismatches due to the misalignment schematically shown in SFig. 13(c), indicating the generality of our observations.

C. Anticrossing between V_B^- Phonons

The large suspended membrane in the sample indeed arises from a break line during the fabrication as shown in SFig. 15(a). In the wet underetching, the KOH solution etches the Si below the large suspended membrane



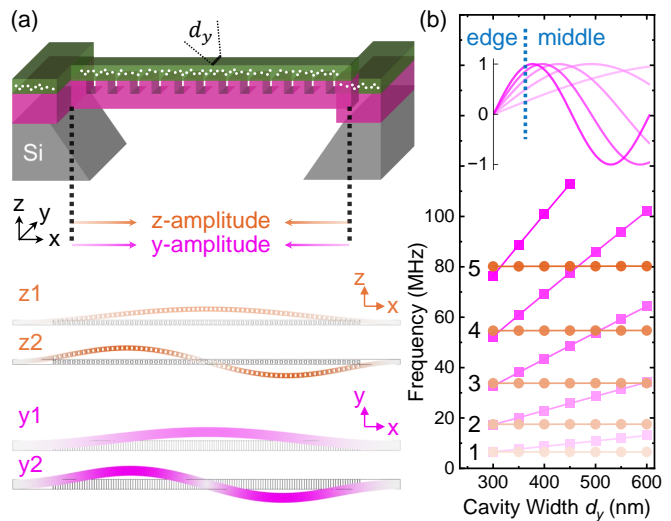
SFig. 15. (a) Left top part of the SEM image in Fig. 2(b). The large suspended membrane arises from a break line during the sample fabrication. (b) Raman map in SFig. 13(a). (c) Raman spectra extracted from the loop trace in (b). (d) Energy of highly localized phonons, revealing the anticrossings between Raman peaks.

through this break line, which is created during the IC-PRIE etching. The out-of-plane vibration has maximum amplitude around this break line, and thereby, the corresponding total PL intensity and Raman intensity of peak 10 are both strongest, as presented in SFig. 13(a)(b).

To avoid discontinuous position dependence from the break line, the two traces used in Fig. 3 both avoid the break line. Here we extract the Raman spectra from the loop trace in SFig. 15(b) (the break line again avoided) and the results are presented in SFig. 15(c). The energy of highly localized phonons are presented in SFig. 15(d). Similar to the PL peaks in Fig. 3(c), anticrossings are observed between the Raman spectra as denoted by the dashed lines. These anticrossings further strengthen the consistence between Raman and PL spectra and support the strong coupling from the Raman point of view.

D. Superposition of Cavity Vibronic Modes

For the case in Fig. 2(b), the effects from y -/ z - vibronic modes can be separated by the comparison between the large suspended membrane and the nanobeam. In contrast, for the nanobeam cavities directly clamped to the non-underetched region (without the large suspended membrane) schematically illustrated in SFig. 16(a), the y -/ z - modes cannot be separated, and the state of motion is a superposition of different modes. We calcu-

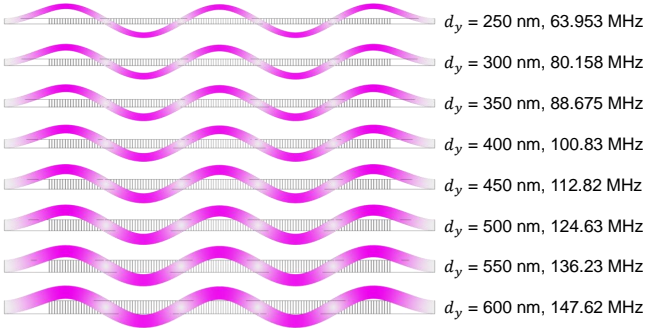


SFig. 16. (a) Schematic of the nanobeam cavity and the y_i and z_j vibronic modes. (b) Calculated vibration frequencies of modes y_1 -5 and z_1 -5. Insets show the vibration profile for modes y_1 -5.

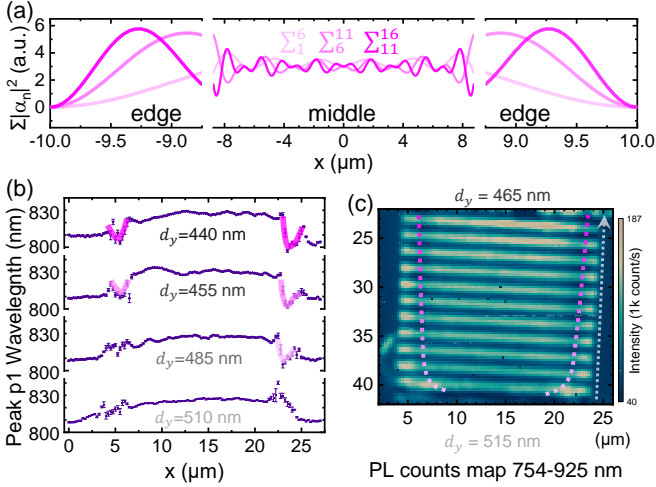
late the nanobeam vibronic modes using the finite element method [5]. The y -/ z - modes are labelled according to the local harmonics (number of anti-nodes). Hereby, the modes are indexed in the figure as y_i and z_j where $i, j \in (1, 2, 3, \dots)$ respectively, such as the z_1 , z_2 , y_1 and y_2 modes plotted in SFig. 16(a).

We have nanobeam cavities with varying width d_y on the sample. The d_y -dependent frequency of y_i and z_j modes are presented in SFig. 16(b). The central result is that the frequency of all y_i modes strongly depends on d_y , while the frequency of all z_j modes rarely changes with d_y . For example, we plot the y_5 mode of cavities with $d_y = 250 - 600$ nm in SFig. 17. This is because the y - (z -) vibration frequencies of a nanobeam depend on the y - (z -) bending rigidity which is determined by the width of nanobeam in y (z) direction d_y (d_z) [22]. In our sample, d_z is fixed by the thickness of hBN and Si_3N_4 , whilst d_y varies between different nanobeam cavities. Therefore, d_y varies the frequency of y_i modes but not z_j modes. Such dependence means that for a given frequency, the harmonic i of corresponding y_i mode will increase as d_y decreases, whilst the harmonic j of corresponding z_j mode is constant. The different modes result in the different vibration amplitude. We plot the profile of y_i modes $i = 1 - 5$ in the inset of SFig. 16(b). As shown, the y -amplitude increases with increasing i (decreasing d_y) at nanobeam edge whilst is complex in the middle region.

We note that the optical and mechanical properties of hBN are not well known yet and strongly depend on the specific flake such as the local defect concentration [23]. In this work, we tentatively use the parameters of Si_3N_4 for the hBN, which means all materials are set to Si_3N_4 in the calculations, to achieve a numerical re-



SFig. 17. Calculated y_5 mode for nanobeam cavities with the varying width d_y .



SFig. 18. (a) The sum amplitude of multiple y_i modes. Σ_1^6 , Σ_6^{11} and Σ_{11}^{16} are the simulation of a broad, medium and narrow cavity, respectively. (b) PL shift of p1 and (c) total PL intensity in nanobeam cavities, corresponding to the bottom part of the SEM image in Fig. 2(b). Magenta lines in (b)(c) denote the blue shift of p1 and the suppression of total PL intensity at nanobeam edges. These are both y -effects and increase as d_y decreases, agreeing perfectly to the theoretical predictions in (a).

sult. This might introduce differences between the calculation and experiment. However, we emphasize that the varying frequencies of y_i modes are due to the bending rigidity changing with the spatial extent in y -direction (d_y) [22]. In contrast, the bending rigidity in z -direction rarely changes, due to the spatial extent in z -direction (thickness of hBN and Si_3N_4) is same for all nanobeams. The geometric dependence of bending rigidity is a fundamental property in mechanics and does not rely on the parameters of specific materials. Therefore, although the absolute value of frequency in the calculation might differ to the experiment, the key which means the different d_y dependence of y -/ z - modes, are always true.

Next, we use the simple trigonometric profiles

$$\alpha_i = \sin(i\pi(x/L + 1/2)) \quad (16)$$

to describe the eigenmodes and predict the superposition of multiple y_i modes. Here, L is the nanobeam length and $x \in (-L/2, L/2)$ is the position relative to the center point [24]. We simulate the interaction effect of the superposition state to V_B^- by summing the amplitude of multiple modes with random phase factors. Strictly, the summed coupling effect $a(x)$ should be

$$a(x) = \sum_f n(f) |g(f) \alpha_f(x)|^2 \quad (17)$$

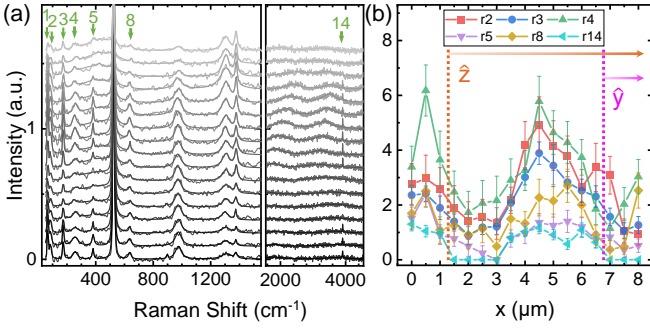
, where α_f is the vibration profile of mode y_i which has the frequency f , $n(f)$ is the Bose factor $n(f) = 1/[e^{hf/(k_B T)} - 1]$ where k_B is the Boltzmann constant, and $g(f)$ reflects the coupling strength to V_B^- . For a given f , the corresponding mode order i changes with the nanobeam width d_y . Meanwhile, $g(f)$ is an intrinsic property of V_B^- and does not change with d_y . Theoretically we could predict the d_y -dependent superposition based on Eq. (17).

However, at this point $g(f)$ is difficult to get by either calculation or experiment. For a simple but qualitative example, we calculate the superposition according to

$$a(x) = \sum_{i \in G} |\alpha_i(x)|^2 \quad (18)$$

where $i \in G$ means the y_i modes have the frequencies within the range G which couples to V_B^- . G is an intrinsic property of V_B^- , and the corresponding harmonics i within G changes with d_y . We assume that for a broad cavity with large d_y , $i \in G = 1 - 6$ thus the superposition (coupling) $a(x) = \Sigma_1^6$. Similarly, for a medium cavity $i \in G = 6 - 11$ and for a narrow cavity $i \in G = 11 - 16$. The three superpositions are presented in Fig. 18(a). As shown, $a(x)$ at nanobeam edge clearly increase as d_y decreases. This is due to the nanobeam edge $x = \pm L/2$ is the node of all modes, thus the sum of multiple y_i modes retains the d_y dependence of each single mode as discussed in the inset of SFig. 16(b). In contrast, in the middle region, the nodes of different modes are interlaced, thereby, the sum exhibits only minor variations. Therefore, based on SFig. 18(a) we can predict that as d_y decreases, the y -effects of V_B^- emission at nanobeam edges become stronger, but the V_B^- emission in the middle of the nanobeam exhibits little position dependence. Meanwhile, the z -effects is not affected by d_y .

The highly simplified approach Eq. (18) is not strictly equal to the correct approach Eq. (17). However, we can expect the result obtained by Eq. (17) would be qualitatively similar to the simple approach Eq. (18), because the two fundamental properties – the nanobeam edge is the node of all modes and the nodes of multiple modes are interlaced in the middle – are always correct and not affected in Eq. (18). Indeed, the theoretical predictions in SFig. 18(a) agree perfectly to the experimental observations as presented in Fig. 18(b)(c). As discussed in the context of Fig. 3, y -vibration blue shifts PL peak p1 and suppresses the PL intensity. The "concave" blue



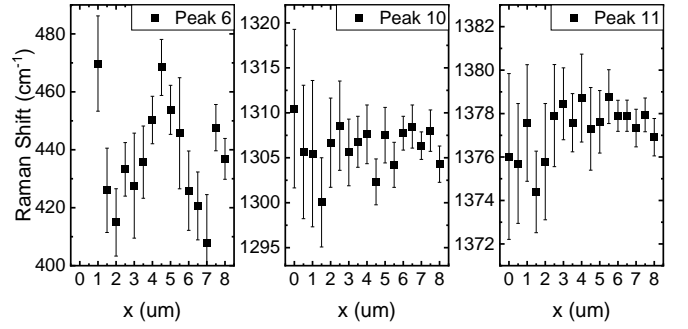
SFig. 19. Raman peaks 1-5, 8 and 14 exhibit few direct relation to the V_B^- emission. (a) Position-dependent Raman spectra, where the right panel is already presented in Fig. 3. (b) Their intensity variation.

shift of PL peak p1 in Fig. 18(b), corresponding to the "convex" y -amplitude predicted in Fig. 18(a), becomes significant as d_y decreases. Meanwhile, from edge to middle the PL intensity is firstly enhanced (z -effect) and then suppressed (y -effect), resulting in the bright bar at nanobeam edges shown in Fig. 18(c). As d_y decreases, the bright bar becomes shorter, indicating stronger suppression from y -vibrations. In contrast to these clear effects at nanobeam edges, the V_B^- emission in the middle region are generally stable but with minor variations. All these results are consistent to predictions in Fig. 18(a). These perfect agreement of d_y dependence between theory and experiment further supports the emitter-optomechanical interaction.

Besides the vibration of whole nanobeam presented in SFig. 18, our cavity also supports the confined vibronic modes (\sim GHz) at the cavity center [5, 25]. In our previous work, we find that the MoS₂ exciton couples to both the beam and confined vibronic modes [5]. In contrast, in most cavities here, no particular change of V_B^- emission wavelength or intensity is observed at the cavity center, as shown in Fig. 18(b)(c). This result might be due to that V_B^- prefers to couple to MHz rather than GHz modes, or the high-frequency modes are degraded by the air since the sample is measured bare in the air as shown in SFig. 2.

E. Other Minor Effects of V_B^- Phonons

Whole-range Raman spectra of Fig. 3(a) are presented in SFig. 19(a) here. The intensity of green labelled peaks 1-5, 8 and 14 are presented in SFig. 19(b). The boundary between the non-underetched region and large suspended membrane (orange dashed line) and the boundary between the large suspended membrane and nanobeam (magenta dashed line) are denoted on the figure. As shown, these peaks exhibit the same position dependence: a suppression at both two boundaries. Meanwhile, they have the energy 67, 86, 174, 256, 382, 638 and 3909 cm^{-1} respectively, and no distinguishable shift



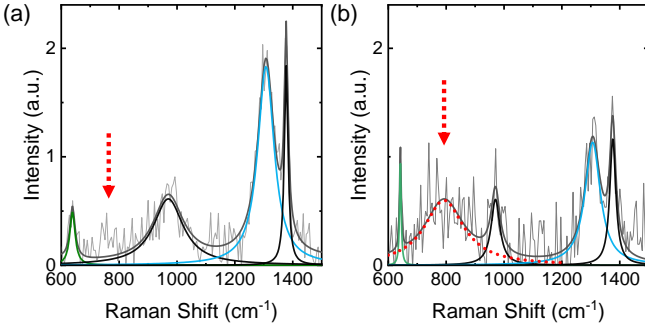
SFig. 20. Energy shifts of Raman peaks 6, 10 and 11, extracted from SFig. 19(a). Peak 6 exhibits distinguishable energy shift, while no distinguishable shift is observed of peaks 10 and 11.

is observed. Comparing to the V_B^- emission (Fig. 3(b)), we find no direct relation of these phonons to either the intensity or the wavelengths of V_B^- emission.

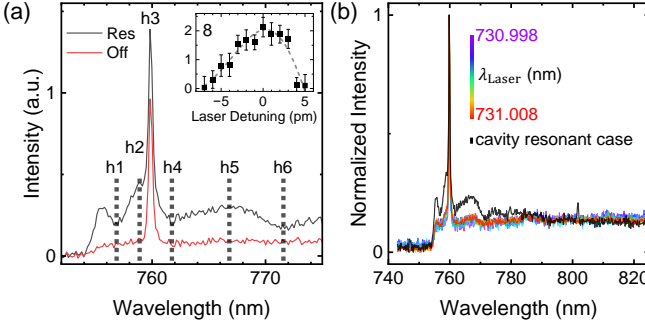
G. Grosso et al. [20] recently reported the study of phonon processes for several nitrogen vacancies in hBN. They found that for nitrogen vacancies, phonons around 150 – 200 meV, which corresponds to the extended phonon peak 10 (162 meV) in this work, dominate the excitation of emitters and determines the total PL intensity. This is same to our observation for the V_B^- centers. Meanwhile, they also found the low-energy acoustic and out-plane optical phonons play few roles in emission of nitrogen vacancies [20]. We observe similar phenomena for the low-energy phonons represented by Raman peaks 1-5. Since peaks 8 and 14 exhibit the same behavior to peaks 1-5, we suggest these phonons are the acoustic or out-plane optical phonons of V_B^- .

In this work, the ultra broad Raman peaks 6, 12 and 13 are the only V_B^- phonons exhibiting distinguishable energy shift. The position-dependent shift of peaks 12 and 13 are already discussed in the main paper. The shift of peak 6 is presented in SFig. 20. Although the fitting is limited by the overlap to other peaks as discussed in Sec. IC, the energy shift is clearly observed. Other phonons such as the extended V_B^- phonon peak 10 and bulk hBN phonon peak 11 presented in SFig. 20 might also be shifted by the position-dependent vibration. However, their shifts are too small, thus we cannot distinguish due to the low signal noise ratio (SNR).

Besides peaks 1-14, in some cases we observe other peaks in the Raman spectra. For example, sometimes we observe another broad peak around 800 cm^{-1} , as shown in SFig. 21, which might be another multi-phonon state of highly localized phonon. However, the SNR of such peaks are very low, and they cannot always be distinguished in the spectra. Therefore, we do not further discuss these minor peaks.



SFig. 21. Raman spectra recorded at two positions in the suspended region. We observe another broad peak around 800 cm^{-1} in some cases.



SFig. 22. (a) Comparison of the spectra at (black) and off (red) resonance. Phonon intensities are extracted by the Raman peak heights. Inset is the height of Raman peak 8 from V_B^- , similar to peak 6 in Fig. 4(b). (b) Control experiments. Color lines are normalized spectra recorded at one position in the large suspended membrane (no photonic mode), with the same laser tuned from 730.998 to 731.008 nm. Black line is the resonant spectra in (a) for comparison.

IV. RESONANT EXCITATION: METHODS AND CONTROL EXPERIMENTS

In the resonant excitation of cavity photons presented in Fig. 4, we use a filter to cut the laser signal. The cutting can be clearly observed in the spectra. Since the Raman peaks are close to the cut wavelength, their signal might be affected by the filter more or less, making the subtracting and fitting of the spectra difficult. Therefore, we extract the peak height for brevity, as shown in SFig. 22(a). We directly extract the data points as denoted by h1-6. The height of Raman peak 6 from V_B^- phonon is calculated by $h_6 = h_2 - h_1$ and peak 7 from

Si_3N_4 by $h_7 = h_3 - h_2$. In addition, we extract the height of peak at 766 nm (h_5) by $h_8 = h_5 - (h_4 + h_6)/2$. For this peak, the Raman shift 625 cm^{-1} generally agrees to the peak 8 but the linewidth is broader. This might originate from the coupling to the cavity optomechanical mode, or the impact of another broad phonon discussed in SFig. 21. Whether which case it is, the major conclusion that V_B^- phonons are enhanced by the coupling to cavity photons, is not affected. The conclusion is strengthened by the control experiment presented in SFig. 22(b). We use the same tunable laser and record the spectra at a position in the large suspended membrane. As expected, no resonant behavior is observed in the control experiment. In addition, the enhancement of Si_3N_4 phonon (Fig. 4(b)) gives a description of the real linewidth (red line) of cavity photonic mode as $3.5 \pm 0.1 \text{ pm}$, providing a solid evidence of Q-factor $> 2 \times 10^5$ in the ultra-high regime [26].

V. ADDITIONAL DISCUSSIONS

In this supplemental material, we present additional discussions to strengthen the conclusions reported in the main paper. Meanwhile, we note that some specific details could be interesting future topics. E.g., besides the y-/z- vibrations, the nanobeam cavity also supports x-vibrations, rotate vibrations and cavity confined vibrations which have much higher frequencies [5, 25]. Since V_B^- will interact with multiple vibrations, it would be an interesting topic to control the vibronic modes separately. Considering the zero-phonon emission of V_B^- at $\sim 773 \text{ nm}$ [4] and the replica peak p1 at $\sim 805 \text{ nm}$ in the non-underetched region, we can expect that peak p1 arises from the zero-phonon state by firstly absorbing an extended phonon peak 10 (1306 cm^{-1}) and then emit a highly localized phonon peak 12 (1800 cm^{-1}). The green labelled phonons also exhibit interaction effect with the vibrations as discussed in Sec. III E. These results indicate more features in the emission dynamics of V_B^- that are not well studied yet.

We suggest that the hyperbolic dispersion of hBN [27] contributes to the phonon-induced emission, since it provides a strong confinement of phonons. Previous works reported that the hyperbolic features can be controlled by nanostructures [28, 29] or even a suspending of hBN flakes [30]. Such controls are similar to the cavity-induced control of V_B^- centers we observed. We believe further investigations would help unveiling more unique emitters and extend the application of this work.

[1] F. Pizzocchero, L. Gammelgaard, B. S. Jessen, J. M. Caridad, L. Wang, J. Hone, P. Bøggild, and T. J. Booth, The hot pick-up technique for batch assembly of van der Waals heterostructures, *Nat. Commun.* **7**, 11894 (2016).
 [2] N.-J. Guo, W. Liu, Z.-P. Li, Y.-Z. Yang, S. Yu, Y. Meng,

Z.-A. Wang, X.-D. Zeng, F.-F. Yan, Q. Li, J.-F. Wang, J.-S. Xu, Y.-T. Wang, J.-S. Tang, C.-F. Li, and G.-C. Guo, Generation of spin defects by ion implantation in hexagonal boron nitride, *ACS Omega* **7**, 1733 (2022).
 [3] C. Qian, V. Villafañe, P. Soubelet, A. Hötger,

- T. Taniguchi, K. Watanabe, N. P. Wilson, A. V. Stier, A. W. Holleitner, and J. J. Finley, Nonlocal exciton-photon interactions in hybrid high- q beam nanocavities with encapsulated mos_2 monolayers, *Phys. Rev. Lett.* **128**, 237403 (2022).
- [4] C. Qian, V. Villafañe, M. Schalk, G. V. Astakhov, U. Kentsch, M. Helm, P. Soubelet, N. P. Wilson, R. Rizzato, S. Mohr, A. W. Holleitner, D. B. Bucher, A. V. Stier, and J. J. Finley, Unveiling the zero-phonon line of the boron vacancy center by cavity-enhanced emission, *Nano Lett.* **22**, 5137 (2022).
- [5] C. Qian, V. Villafañe, P. Soubelet, A. V. Stier, and J. J. Finley, Exciton coupling with cavity vibrational phonons and mos_2 lattice phonons in hybrid nanobeam cavities (2022), [arXiv:2204.04304](https://arxiv.org/abs/2204.04304).
- [6] E. E. Diel, J. W. Lichtman, and D. S. Richardson, Tutorial: avoiding and correcting sample-induced spherical aberration artifacts in 3d fluorescence microscopy, *Nat. Protoc.* **15**, 2773 (2020).
- [7] K. R. Spring and M. W. Davidson, Spherical aberration from coverslip thickness variations.
- [8] M. Aspelmeyer, T. J. Kippenberg, and F. Marquardt, Cavity optomechanics, *Rev. Mod. Phys.* **86**, 1391 (2014).
- [9] J. Zhou, J. Zheng, Z. Fang, P. Xu, and A. Majumdar, Ultra-low mode volume on-substrate silicon nanobeam cavity, *Opt. Express* **27**, 30692 (2019).
- [10] J. Guo and S. Gröblacher, Integrated optical-readout of a high- q mechanical out-of-plane mode, *Light: Sci. Appl.* **11**, 282 (2022).
- [11] J. Vučković, Quantum optics and cavity qed with quantum dots in photonic crystals (Oxford University Press, Oxford, 2017) pp. 365–406.
- [12] M. Nomura, N. Kumagai, S. Iwamoto, Y. Ota, and Y. Arakawa, Laser oscillation in a strongly coupled single-quantum-dot–nanocavity system, *Nat. Phys.* **6**, 279 (2010).
- [13] J. Jimenez-Mier, Contribution of the instrument window function to the profile of autoionizing resonances, *J. Quant. Spectrosc. Radiat. Transfer* **51**, 741 (1994).
- [14] M. Tsuchiya, S. K. Sankaranarayanan, and S. Ramanathan, Photon-assisted oxidation and oxide thin film synthesis: A review, *Prog. Mater. Sci.* **54**, 981 (2009).
- [15] P. Yao, P. K. Pathak, E. Illes, S. Hughes, S. Münch, S. Reitzenstein, P. Franeck, A. Löffler, T. Heindel, S. Höfling, L. Worschech, and A. Forchel, Nonlinear photoluminescence spectra from a quantum-dot–cavity system: Interplay of pump-induced stimulated emission and anharmonic cavity qed, *Phys. Rev. B* **81**, 033309 (2010).
- [16] V. Ivády, G. Barcza, G. Thiering, S. Li, H. Hamdi, J.-P. Chou, Ö. Legeza, and A. Gali, Ab initio theory of the negatively charged boron vacancy qubit in hexagonal boron nitride, *npj Comput. Mater* **6**, 41 (2020).
- [17] J. R. Reimers, J. Shen, M. Kianinia, C. Bradac, I. Aharonovich, M. J. Ford, and P. Piecuch, Photoluminescence, photophysics, and photochemistry of the V_B^- defect in hexagonal boron nitride, *Phys. Rev. B* **102**, 144105 (2020).
- [18] F. Libbi, P. M. M. C. de Melo, Z. Zanolli, M. J. Verstraete, and N. Marzari, Phonon-assisted luminescence in defect centers from many-body perturbation theory, *Phys. Rev. Lett.* **128**, 167401 (2022).
- [19] I. Wilson-Rae and A. Imamoglu, Quantum dot cavity-qed in the presence of strong electron-phonon interactions, *Phys. Rev. B* **65**, 235311 (2002).
- [20] G. Grosso, H. Moon, C. J. Ciccarino, J. Flick, N. Mendelson, L. Mennel, M. Toth, I. Aharonovich, P. Narang, and D. R. Englund, Low-temperature electron–phonon interaction of quantum emitters in hexagonal boron nitride, *ACS Photonics* **7**, 1410 (2020).
- [21] T. Yang, N. Mendelson, C. Li, A. Gottscholl, J. Scott, M. Kianinia, V. Dyakonov, M. Toth, and I. Aharonovich, Spin defects in hexagonal boron nitride for strain sensing on nanopillar arrays, *Nanoscale* **14**, 5239 (2022).
- [22] D. Hoch, X. Yao, and M. Poot, Geometric tuning of stress in predisplaced silicon nitride resonators, *Nano Lett.* **22**, 4013 (2022).
- [23] S. Thomas, K. M. Ajith, S. Chandra, and M. C. Valsakumar, Temperature dependent structural properties and bending rigidity of pristine and defective hexagonal boron nitride, *J. Phys.: Condens. Matter* **27**, 315302 (2015).
- [24] H. B. Khaniki, M. H. Ghayesh, R. Chin, and S. Husain, Nonlinear continuum mechanics of thick hyperelastic sandwich beams using various shear deformable beam theories, *Continuum Mech. Thermodyn.* **34**, 781 (2022).
- [25] M. Eichenfield, J. Chan, R. M. Camacho, K. J. Vahala, and O. Painter, Optomechanical crystals, *Nature* **462**, 78 (2009).
- [26] B.-S. Song, S. Noda, T. Asano, and Y. Akahane, Ultra-high- q photonic double-heterostructure nanocavity, *Nat. Mater.* **4**, 207 (2005).
- [27] S.-A. Biehs, M. Tschikin, and P. Ben-Abdallah, Hyperbolic metamaterials as an analog of a blackbody in the near field, *Phys. Rev. Lett.* **109**, 104301 (2012).
- [28] J. D. Caldwell, A. V. Kretinin, Y. Chen, V. Giannini, M. M. Fogler, Y. Francescato, C. T. Ellis, J. G. Tischler, C. R. Woods, A. J. Giles, M. Hong, K. Watanabe, T. Taniguchi, S. A. Maier, and K. S. Novoselov, Sub-diffractive volume-confined polaritons in the natural hyperbolic material hexagonal boron nitride, *Nat. Commun.* **5**, 5221 (2014).
- [29] P. Pons-Valencia, F. J. Alfaro-Mozaz, M. M. Wiecha, V. Bielek, I. Dolado, S. Vélez, P. Li, P. Alonso-González, F. Casanova, L. E. Hueso, L. Martín-Moreno, R. Hilenbrand, and A. Y. Nikitin, Launching of hyperbolic phonon-polaritons in h-bn slabs by resonant metal plasmonic antennas, *Nat. Commun.* **10**, 3242 (2019).
- [30] S. Dai, J. Quan, G. Hu, C.-W. Qiu, T. H. Tao, X. Li, and A. Alù, Hyperbolic phonon polaritons in suspended hexagonal boron nitride, *Nano Lett.* **19**, 1009 (2019).